

# Hydrodynamical simulations of cluster formation with central AGN heating

D. Sijacki<sup>\*</sup> and V. Springel

*Max-Planck-Institut für Astrophysik, Karl-Schwarzschild-Straße 1, 85740 Garching bei München, Germany*

6 September 2018

## ABSTRACT

We analyse a hydrodynamical simulation model for the recurrent heating of the central intracluster medium (ICM) by active galactic nuclei (AGN). Besides the self-gravity of the dark matter and gas components, our approach includes the radiative cooling and photoheating of the gas, as well as a subresolution multiphase model for star formation and supernova feedback. Additionally, we incorporate a periodic heating mechanism in the form of hot, buoyant bubbles, injected into the intragalactic medium (IGM) during the active phases of the accreting central AGN. We use simulations of isolated cluster halos of different masses to study the bubble dynamics and the heat transport into the IGM. We also apply our model to self-consistent cosmological simulations of the formation of galaxy clusters with a range of masses. Our numerical schemes explore a variety of different assumptions for the spatial configuration of AGN-driven bubbles, for their duty cycles and for the energy injection mechanism, in order to obtain better constraints on the underlying physical picture. We argue that AGN heating can substantially affect the properties of both the stellar and gaseous components of clusters of galaxies. Most importantly, it alters the properties of the central dominant (cD) galaxy by reducing the mass deposition rate of freshly cooled gas out of the ICM, thereby offering an energetically plausible solution to the cooling flow problem. At the same time, this leads to reduced or eliminated star formation in the central cD galaxy, giving it red stellar colours as observed.

**Key words:** methods: numerical – galaxies: clusters: general – cooling flows – cosmology: theory.

## 1 INTRODUCTION

Clusters of galaxies are the largest virialised objects in the Universe and are thought to contain a representative fraction of baryons (White et al., 1993). Most of these baryons can be found in the diffuse gas of the intracluster medium (ICM), which is directly observable in X-rays, making clusters of galaxies an almost ideal laboratory for studying the physical processes that shape galaxies and halos in the Universe. Clusters of galaxies are also a useful cosmological probe (for a recent review see Voit, 2004), and therefore have been a prime target for theoretical modelling early on, both numerically and analytically.

A first order approximation for the ICM is to represent it as an ideal, non-radiative gas. This leads to the predications of scale invariant relations between X-ray luminosity, mass and temperature (Kaiser, 1986). However, it has long been established that the observed relations do not agree

in detail with these assumptions, e.g. the observed  $L_X$ – $T$  relation is much steeper than expected based on this simple model. In addition, recent observations with radio and X-ray telescopes have revealed a stunning complexity of the ICM physics, including phenomena such as cold fronts, radio ghosts, cluster turbulence, and apparently nearly uniform enrichment to high metallicity.

However, possibly the most puzzling observational fact is the “cooling-flow” problem. Since the cooling time in the central regions of galaxy clusters is smaller than the age of the clusters themselves, a central inflow of cool gas is expected to occur (e.g. Fabian & Nulsen, 1977; Cowie & Binney, 1977; Fabian, 1994). The rate of gas cooling can be estimated by energetic arguments if one assumes that X-ray cooling radiation is fed by the thermal reservoir of the hot cluster plasma. Based on this, the estimated rate of accretion onto the central galaxy is rather high in many cases (e.g. Fabian et al., 1984; White et al., 1994, 1997; Allen, 2000; Allen et al., 2001a), implying that a significant amount of gas cooler than 1 – 2 keV should be present in the centre. How-

<sup>\*</sup> E-mail: deboras@mpa-garching.mpg.de

ever, up to the present time, optical and X-ray observations have failed to detect the required amount of this cool gas, suggesting that it is simply not there (e.g. McNamara et al., 2000; Peterson et al., 2001; Tamura et al., 2001; Balogh et al., 2001; Kaastra et al., 2001; Edge, 2001; Edge et al., 2002; Edge & Frayer, 2003; Fabian et al., 2001; Böhringer et al., 2002; Peterson et al., 2003; Salomé & Combes, 2004). The low current star formation rates of central galaxies (e.g. O’Connell & McNamara, 1989; Johnstone et al., 1987; Allen et al., 1995) provide additional support for the absence of strong cooling flows. Apparently, there must be a physical process that offsets the radiative cooling in the centre, preventing the gas from falling out of the ICM in a cooling flow.

Theoretical studies have therefore often invoked some sort of non-gravitational heating to explain the cluster scaling relations (e.g. Kaiser, 1991; Navarro et al., 1995; Bower, 1997; Tozzi & Norman, 2001; Borgani et al., 2001; Voit & Bryan, 2001; Babul et al., 2002; Voit et al., 2002, 2003; Oh & Benson, 2003; Tornatore et al., 2003; Borgani et al., 2004). The main unsolved issue in these models remains the origin and nature of the physical sources that cause the extra-heating of the ICM. Perhaps the most obvious heat source is supernovae associated with star formation, but it seems questionable that they are able to supply the required amount of feedback energy. Curiously, radiative cooling alone may also account for the steepness of the  $L_X$ - $T$  relation by eliminating gas more efficiently in low-mass systems (e.g. Lewis et al., 2000; Voit & Bryan, 2001; Muanwong et al., 2001; Yoshida et al., 2002; Wu & Xue, 2002; Voit et al., 2002; McCarthy et al., 2004), but this produces a drastic overprediction of the amount of cold gas (apart from a problem with the  $L_X$ - $T$  zero-point) and is therefore disfavoured. Models that self-consistently incorporate SNe heating and radiative cooling processes are also only found to have limited success (e.g. Borgani et al., 2004). The over-cooling problem therefore remains unsolved. Another problem is posed by simulated temperature profiles, which typically exhibit a trend to increase towards the cluster centre, in disagreement with observational inferences (e.g. Allen et al., 2001b; De Grandi & Molendi, 2002).

An array of different physical hypothesis have been proposed to solve the cooling-flow paradox, including thermal conduction, magnetic fields, cosmic rays, and hot buoyant bubbles from AGN jets. Thermal conduction may in principle offset central cooling losses by inducing a heat current from outer, hotter regions of clusters (e.g. Narayan & Medvedev, 2001), provided the conductivity is not strongly suppressed by tangled magnetic fields. Analysis of static cluster models with conduction have been able to provide good matches to observed temperature profiles in some cases (e.g. Voigt et al., 2002; Zakamska & Narayan, 2003; Voigt & Fabian, 2003) but detailed self-consistent numerical simulations which followed conduction still encountered the cooling flow problem (e.g. Jubelgas et al., 2004; Dolag et al., 2004), making it questionable whether this can be the real solution.

The more widely favoured hypothesis is instead that the central AGN may supply the required amount of energy. Accretion onto supermassive black holes is thought to liberate of order  $\sim 10\%$  of the accreted rest mass energy, implying that even for low accretion rates onto a supermassive black hole, offsetting the cooling flows is energetically quite possi-

ble. In fact, such accretion powers high-redshift quasars, the most luminous sources in the universe. Quasar activity is likely to be triggered by mergers of galaxies, where cold gas is forced to the nuclei by gravitational tidal forces. This accretion and the associated quasar feedback has recently been incorporated into simulations, and shown to play a potentially important role in shaping the properties of elliptical galaxies (Springel et al., 2005a).

In clusters of galaxies, however, it seems clear that the central AGN activity that causes bubbles is of a different nature, and needs not be triggered by galaxy mergers. Observationally, many clusters of galaxies show evidence for X-ray cavities filled with radio plasma (e.g. Owen et al., 2000; Blanton et al., 2001), which are thought to be inflated by relativistic jets from the AGN. Theoretically, it has been shown that these bubbles may rise buoyantly and raise some of the central cool gas (e.g. Churazov et al., 2001), allowing it to mix with the hotter gas further out. Together with the accompanying mechanical and possibly viscous heating, this can then constitute an efficient feedback mechanism.

In this paper, we focus on the phenomenology of this bubble feedback, without addressing the small scale physics of the accretion onto the black hole. This extends earlier simulation studies which all employed hydrodynamical mesh codes, but which focused exclusively on highly idealised cluster models (e.g. Churazov et al., 2001; Quilis et al., 2001; Ruszkowski & Begelman, 2002; Churazov et al., 2002; Brüggén et al., 2002; Brüggén & Kaiser, 2002; Brüggén, 2003; Nulsen et al., 2003; Dalla Vecchia et al., 2004; Hoeft & Brüggén, 2004). A first goal of our work is to demonstrate that such simulations are also possible with the smoothed particle hydrodynamics (SPH) technique, and give results consistent with earlier studies. This is important because the Lagrangian nature of SPH is ideal for cosmological simulations of structure formation, and if applicable for bubble feedback, will allow us to carry out the first self-consistent cosmological simulations with AGN-driven bubble heating. An equally important goal of our simulations is to gain new insights into the efficiency of bubble feedback associated with AGN for modifying the thermodynamic state of the ICM and the properties of cluster galaxies over the course of cosmic history. Our modelling can hence inform semi-analytic models of galaxy formation that have just begun to include AGN feedback (e.g. Croton et al., 2005), and provide crucial input for future hydrodynamic simulations that try to incorporate the growth of supermassive black holes both from the quasar- and the radio-mode.

The outline of this paper is as follows. In Section 2, we describe the characteristics of our simulation code and the numerical method adopted to introduce bubble heating. In Section 3 we analyse the AGN heating in isolated galaxy halos, spanning a wide range in mass, and we present some Chandra-like photon images of simulated bubbles. The effects of AGN heating in cosmological simulations of galaxy cluster formation is discussed in Section 4. Finally, in Section 5 we discuss successes and limitations of our model, and we present our conclusions.

## 2 METHODOLOGY

### 2.1 Basic code properties

Our simulations have been performed with the parallel TreeSPH-code GADGET-2 (Springel, 2005; Springel et al., 2001b). We use the ‘entropy formulation’ for SPH suggested by Springel & Hernquist (2002), which manifestly conserves both energy and entropy when adaptive smoothing lengths are used. Besides gravitational and hydrodynamical processes, we include radiative cooling of the gas component, together with heating by a spatially uniform, time dependent UV background modelled as in Katz et al. (1996). The gas consists of an optically thin primordial plasma of hydrogen and helium. In addition, a multiphase subresolution model for the treatment of star formation and associated feedback mechanisms has been adopted (Springel & Hernquist, 2003). In this model, stars form from dense cold gas clouds assumed to reside at pressure equilibrium in a surrounding hot phase of the interstellar medium. Supernova explosions heat the hot medium and evaporate cold clouds, thereby providing a self-regulation cycle for star formation, and a net pressurisation for the highly overdense ISM. Additionally, we use a simple prescription for metal enrichment, which assumes that each star-forming gas element can be locally approximated by a closed box model in which perfect and instantaneous mixing of metals between cold clouds and ambient gas occurs, as explained in detail in Springel & Hernquist (2003).

### 2.2 Phenomenological description of AGN heating in clusters

Besides considering the physical processes already implemented in GADGET-2, we have implemented for this study a new model that accounts for heating by the central AGN in clusters of galaxies. This model does not attempt to provide a fully self-consistent ab initio treatment of the complex physical processes related to accretion onto supermassive black holes in clusters and the associated AGN activity. Rather, we try to mimic the observed phenomenology of hot bubbles in clusters directly in our simulations, without addressing the jet physics that presumably inflates the bubbles in the first place. We therefore assume as a starting point that such bubbles are generated during phases in which an AGN is “switched on”, and introduce them into the IGM in a phenomenological fashion. This allows us to study how the bubbles affect the properties of the central ICM as a function of their characteristics, in particular with respect to distributing their energy content to the surrounding cooler gas.

For definiteness, we assume in our model that a certain amount of thermal energy is injected in the form of centrally concentrated bubbles spaced in uniform time intervals. We parameterise this scheme in terms of the AGN duty cycle, the amount of energy  $E_{\text{bub}}$  injected, and by the radius  $R_{\text{bub}}$  and distance  $d_{\text{bub}}$  of the buoyant bubbles from the cluster centre, respectively.

We first test our scheme for AGN-heating on isolated, axisymmetric halo models. These systems are clean laboratories which permit us to compare directly with analogous modelling in the literature (e.g. Churazov et al., 2001;

Quilis et al., 2001; Dalla Vecchia et al., 2004), and hence to evaluate whether SPH is suitable for such simulations. Moreover, these simplified models give us the possibility to explore straightforwardly and with comparatively low computational cost a large number of cases. In this way we can investigate the importance of different physical parameters of the bubbles, thus constraining their dynamical evolution and the heat transport into the ICM.

As a second step, we apply the model for bubble heating to fully self-consistent cosmological simulations of galaxy cluster formation. Here, we also investigate different redshift-dependent energy injection schemes, allowing us to gain some insight in how the AGN activity influences the hierarchical galaxy cluster growth and the characteristics of the central cluster galaxy, and to elucidate the relative importance of AGN heating with respect to the other physics included. We consider a set of galaxy clusters spanning a range in mass because we expect the efficiency of bubble heating to have a significant mass dependence.

Both for isolated halos and in cosmological simulations, we explored two different schemes for spatially placing the bubbles around the cluster centres. In the first scheme, the bubbles are introduced randomly within a sphere with a radius given by  $d_{\text{bub}}$  around the centre, while in the second approach, two symmetric bubbles are placed randomly along a fixed axis of length  $2 \times d_{\text{bub}}$ , which has an orientation preserved in time during subsequent bubble events. The latter hence mimics a situation where the AGN jet that inflates the bubbles has directional stability over time, which could arise due to some coupling with the host galaxy’s angular momentum, for example. At the present time there is no clear evidence either way concerning what is the preferred scenario, therefore our main aim is to investigate the possible differences in the ICM properties between these two bracketing scenarios.

### 2.3 Constraining the model parameters

Our choice for the values of  $R_{\text{bub}}$  and  $d_{\text{bub}}$  has been guided by observational constraints on X-ray cavities in clusters, and also by the values typically adopted in previous numerical works, for easier comparison. For simplicity, we restricted most of our simulations to the case where the values of  $R_{\text{bub}}$  and  $d_{\text{bub}}$  depend only on the mass of the halo under consideration, and on the redshift in the case of cosmological simulations. Specifically, we adopted

$$R_{\text{bub}} \propto M_{200}(z)^{1/3} \times \frac{1+z}{(\Omega_{0m}(1+z)^3 + \Omega_{0\Lambda})^{1/3}}, \quad (1)$$

where  $M_{200}(z)$  is the virial mass of the host galaxy cluster at given redshift of AGN activity, and the same scaling has been adopted for  $d_{\text{bub}}$ . For the simulations of isolated halos, we used the same dependence of  $R_{\text{bub}}$  and  $d_{\text{bub}}$  on cluster mass, setting  $z = 0$ .

We study multiple bubble injection events in order to analyze how AGN heating couples with radiative cooling losses over a sufficiently long time interval. Thus, our modeling requires prescriptions both for the AGN duty cycle and for the time evolution of the energy content stored in the bubbles. However, most of the observed AGN-driven bubbles are found at low redshifts (e.g. Birzan et al., 2004), and only recently some observational evidence for X-ray cavities

in more distant galaxy clusters has been found (McNamara et al., 2005). Therefore, the properties and presence of radio-bubbles at higher redshifts, and their evolution with time, are observationally rather unconstrained. We hence limit ourselves in this work to simple parametric prescriptions for the evolution of  $E_{\text{bub}}$ , derived from basic theoretical considerations and empirical laws, which hopefully bracket reality. Typically, we started injecting bubbles at redshift  $z = 3$ , which is the epoch that roughly corresponds to the peak of the comoving quasar space density, but we also tested an earlier epoch given by  $z = 6$  for the start of the bubble activity. For our modeling of the evolution of  $E_{\text{bub}}$  with time, we adopted two scenarios with rather different behaviour. In the first one, most of the energy is released at late epochs, while in the second one, the bubble energy is coupled more closely to an assumed BH accretion rate (BHAR) model for the growth of the black hole population as a whole, such that the energy release is more pronounced at high redshifts.

More specifically, our first model is loosely motivated by the Magorrian relationship, which implies  $M_{\text{BH}} \propto \sigma^4$ . A relation between the bubble mechanical luminosity and the black hole accretion rate,  $\dot{M}_{\text{BH}}$ , can be derived by assuming that only a small fraction of the total bolometric luminosity thermally couples with the ICM. Hence,  $L_{\text{bub}} = f \times L_{\text{bol}} = f \times \epsilon \dot{M}_{\text{BH}} c^2$ . The factor  $f$  sets the efficiency of thermal coupling with the ICM, and is typically assumed to lie in the range of 1-5%, while  $\epsilon$  is the radiative efficiency factor. Assuming that the mechanical luminosity for Eddington-limited accretion is directly proportional to the black hole mass, the energy content  $E_{\text{bub}}$  of the bubbles is then proportional to  $M_{200}(z)^{4/3}$ , provided the mass of the central cluster galaxy scales self-similarly with the cluster mass. Hence, it follows that in this model the bubble energy content is determined by the mass assembly of the host galaxy cluster with time.

In our second scenario, we instead relate the amount of bubble energy to the average growth rate of supermassive central black holes. To describe the latter, we employ an estimate of the BHAR by Di Matteo et al. (2003), who give an analytic fit

$$\dot{\rho}(z) = \epsilon_{\text{BH}} \frac{b \exp[a(z - z_m)]}{b - a + a \exp[b(z - z_m)]}, \quad (2)$$

for their numerical results, with the parameters  $a = 5/4$ ,  $b = 3/2$ ,  $z_m = 4.8$ , and  $\epsilon_{\text{BH}} = 3 \times 10^{-4} M_{\odot} \text{ yr}^{-1} \text{ Mpc}^{-3}$ . Thus, for every duty cycle of AGN activity we can directly relate  $\dot{M}_{\text{BH}}$  with  $E_{\text{bub}}$  in the following way,

$$\frac{E_{\text{bub}}}{E_{\text{norm}}} = f \times \epsilon \times c^2 \int_{z_1}^{z_2} \dot{\rho}(z) dz, \quad (3)$$

where a normalisation factor,  $E_{\text{norm}}$ , has been introduced which we set such that the total energy injected over all duty cycles is the same in our two schemes. We note that the different temporal evolution of the BH mass in this approach implies a significantly reduced energy content of the bubbles at low redshifts. Finally, there is still one free constant of integration which we choose by requiring that the assumed mass of the black hole is the same at  $z = 0$  in both scenarios.

A number of observational and theoretical works (e.g. Birzan et al., 2004; Sanderson et al., 2005; McNamara et al., 2005; Nulsen et al., 2005a,b; Donahue et al., 2005; Voit &

Donahue, 2005) have constrained the plausible time interval between two successive bubble injection episodes to be of order of  $\Delta t_{\text{bub}} \sim 10^8 \text{ yrs}$ . Clearly,  $\Delta t_{\text{bub}}$  could vary both for clusters of different mass and also in time, especially if the bubble activity is triggered by a self-regulated mechanism that operates between AGN feedback and the cooling flow. Nevertheless, given our simple phenomenological approach and lack of any better observational constraints, we adopt the value of  $\Delta t_{\text{bub}} = 10^8 \text{ yrs}$  for all of our cluster simulations, independent of the cosmological epoch.

While some of our prescriptions for bubble parameters are motivated by “quasar-like” phenomena, our models are really meant to reflect a mode of feedback by supermassive black holes different from that of ordinary quasars. Instead of being triggered by mergers and being fueled with dense and cold ISM gas, the bubbles are a model for the radio activity observed in clusters. Note that there are also newly emerging theoretical models (e.g. Croton et al., 2005; Churazov et al., 2005) on how both quasar activity at higher redshifts and AGN-driven radio bubbles at lower redshifts can be described within a common unified framework. We will discuss this possibility in more detail in our conclusions.

### 3 AGN HEATING OF ISOLATED GALAXY CLUSTERS

We here analyse simulations of isolated halos, consisting of a static NFW dark matter halo (Navarro et al., 1996, 1997) with a gaseous component that is initially in hydrostatic equilibrium and chosen to follow a density distribution similar to the NFW dark matter profile, but slightly softened at the centre according to

$$\rho_g(r) = \frac{f_b \delta_0 \rho_{\text{crit}}}{(r + r_0)/r_s (1 + r/r_s)^2}, \quad (4)$$

where  $r_0$  is a parameter introduced to mimic a gas core radius. The baryonic fraction is given by  $f_b$ , while  $\rho_{\text{crit}}$  is the critical density,  $\delta_0$  is the characteristic overdensity and  $r_s$  is the scale radius. The gas follows the equation of state of an ideal monoatomic gas with adiabatic index  $\gamma = 5/3$ . Besides, a certain amount of angular momentum has been imposed that can be quantified by the dimensionless spin parameter of a halo,

$$\lambda = \frac{J|E|^{1/2}}{GM^{5/2}}, \quad (5)$$

where  $J$  represents the angular momentum,  $M$  is the halo mass, and  $E$  its total energy.

The boundary conditions were chosen to be vacuum, i.e. both density and pressure are initially zero outside the virial radius (defined here as the radius enclosing a mean density equal to  $200 \rho_{\text{crit}}$ ). We have simulated halos with a wide range of masses, with virial radii and concentration parameters as listed in Table 1. The baryonic fraction,  $f_b = 0.12$ , the spin parameter,  $\lambda = 0.05$ , and  $r_0 = 0.02 R_{200}$  were kept fixed for all the halos. When evolved without radiative cooling, these initial models are perfectly stable for more than 1/4 of the Hubble time, as we explicitly checked. This is the timespan we subsequently consider in all our non-trivial simulations, both for the case with cooling and star formation only, and also for the case with additional AGN heating.

| $M_{200} [h^{-1}M_{\odot}]$ | $R_{200} [h^{-1}\text{kpc}]$ | $c$  | $N_{\text{gas}}$ | $m_{\text{gas}} [h^{-1}M_{\odot}]$ | $\epsilon [h^{-1}\text{kpc}]$ |
|-----------------------------|------------------------------|------|------------------|------------------------------------|-------------------------------|
| $10^{12}$                   | 206                          | 12.0 | $3 \times 10^5$  | $4.0 \times 10^5$                  | 1.0                           |
| $10^{13}$                   | 444                          | 6.5  | $3 \times 10^5$  | $4.0 \times 10^6$                  | 2.0                           |
| $10^{14}$                   | 957                          | 8.0  | $3 \times 10^5$  | $4.0 \times 10^7$                  | 5.0                           |
| $10^{15}$                   | 2063                         | 5.0  | $3 \times 10^5$  | $4.0 \times 10^8$                  | 10.0                          |
| $10^{15}$                   | 2063                         | 5.0  | $1 \times 10^6$  | $1.2 \times 10^8$                  | 6.5                           |

**Table 1.** Numerical parameters of the isolated galaxy clusters. The first two columns give the virial mass and radius of the halos, evaluated at  $200\rho_{\text{crit}}$ . The assumed values for the concentration parameter are in the third column, while the initial number and the mass of the gas particles is shown in the fourth and the fifth columns, respectively. The mass of the star particles is half that of the gas particles, because we set the number of generations of star particles that a gas particle may produce to two. Note that there are no parameters for the dark matter particles in these run, because we modelled the dark halo with a static NFW potential. Finally, in the last column, the gravitational softening length  $\epsilon$  for the gas and star particles is given.

For the  $10^{15}h^{-1}M_{\odot}$  isolated cluster, our fiducial set of AGN heating parameters is (if not explicitly stated otherwise)  $E_{\text{bub}} = 5 \times 10^{60}$  erg,  $R_{\text{bub}} = 30h^{-1}\text{kpc}$ ,  $d_{\text{bub}} = 50h^{-1}\text{kpc}$ , and a duty cycle of  $\Delta t_{\text{bub}} = 10^8$  yrs, all kept fix in time. The thermal energy injected in the form of bubbles has been estimated using the simple relations given in Section 2, assuming a  $\sim (5 \times 10^8 - 3 \times 10^9)M_{\odot}$  black hole in the cluster centre (depending on the thermal-coupling efficiency factor  $f$ ). For the halos of lower mass, we assumed that the thermal content of the bubble is proportional to  $M_{200}^{4/3}$ , in analogy to our first scenario for scaling the bubble energy in a cosmological setting. This energy scaling is motivated by the well established observational relation between the black hole mass and the velocity dispersion of the stellar component of the bulge (e.g. Tremaine et al., 2002), given by

$$M_{\text{BH}} = (1.5 \pm 0.2) \times 10^8 M_{\odot} \left( \frac{\sigma}{200 \text{ km s}^{-1}} \right)^{4.02 \pm 0.32}, \quad (6)$$

and on the hypothesis that the central cluster galaxy scales self-similarly with the mass of the cluster itself. Even though these assumptions are certainly very restrictive, they provide us with a definite model that allows a straightforward interpretation of the trends with mass, and supply some guidance for what to expect in full cosmological simulations. We also note that the recent numerical work of Di Matteo et al. (2003) suggests that, once the  $M_{\text{BH}} - \sigma$  relation is established with time, the black hole mass is proportional to  $M_{\text{DM}}^{4/3}$  of the host galaxy.

### 3.1 AGN heating of a massive galaxy cluster

In this section we concentrate on the effects of bubble heating on an isolated galaxy cluster of mass  $10^{15}h^{-1}M_{\odot}$ , while we will discuss the relative importance of AGN heating as a function of mass in the next section. In Figures 1 and 2, we show maps of the projected mass-weighted temperature of the  $10^{15}h^{-1}M_{\odot}$  galaxy cluster, focusing on the central regions in order to highlight the morphology of the bubbles with different injection schemes and at various evolutionary stages. Both figures were obtained for simulations with cooling and star formation, and with AGN feedback of the same strength. However, in the left panel of Figure 1, the bubbles were placed randomly within a sphere of radius  $d_{\text{bub}}$ , while the remaining three panels illustrate the case of two sym-

metrical bubbles injected simultaneously, containing half of the energy each, and with the injection axis preserved with time for different bubble cycles.

In Figure 2, we show results for simulations with the same feedback energy as in Figure 1, but this time the initial radius of the bubbles was two times larger and equal to  $60h^{-1}\text{kpc}$ . After being injected, the bubbles rise due to buoyancy and start to assume more elongated, ‘‘pancake-like’’ shapes, as clearly visible in the left panel of Figure 1. They continue to rise until the surrounding gas entropy becomes comparable to their entropy content, at which point they settle into an equilibrium and dissolve slowly with time. While rising, they push the intracluster gas above them, and also entrain some of the cooler central gas, transporting it to larger radii.

A closer comparison of Figures 1 and 2 makes it clear that the smaller bubbles with their significantly higher energy per particle result in more pronounced mushroom-like structures. Nevertheless, they do not shock the surrounding gas which, on the very top of the bubbles, forms cold rims. At late evolutionary stages, corresponding roughly to a quarter of the Hubble time, (see the right panel of Figure 2), a characteristic bipolar outflow is visible as a result.

In Figure 3, we analyse the global gas properties of the cluster in terms of radial profiles of density, temperature and entropy of the hot gas component, i.e. gas of the cold interstellar medium is not included in the plots\*. Bubble injection modifies the inner  $100h^{-1}\text{kpc}$  substantially, reducing the density and increasing the temperature profile. Accordingly, the entropy of the central gas particles is changed as well, and an entropy floor is formed. The lower right panel of Figure 3 shows the mean gas inflow rate in the central  $30h^{-1}\text{kpc}$ . After a relatively brief period of time, AGN heating regulates, in a stable fashion, the flow of gas towards the centre, preventing the unrealistically high mass deposition rates of a fully developed cooling flow, which can reach up to  $1200M_{\odot}\text{yr}^{-1}$  in the case without bubble heating. Even though a repeated injection of bubbles along the same spatial axis (‘‘jet-like’’) is somewhat more efficient than a random placement within a sphere, the gas profiles have very similar trends in both cases, indicating the robustness of the

\* The ‘cold’ gas component has been defined here as all gas cooler than 1keV and with a density higher than the star formation density threshold.

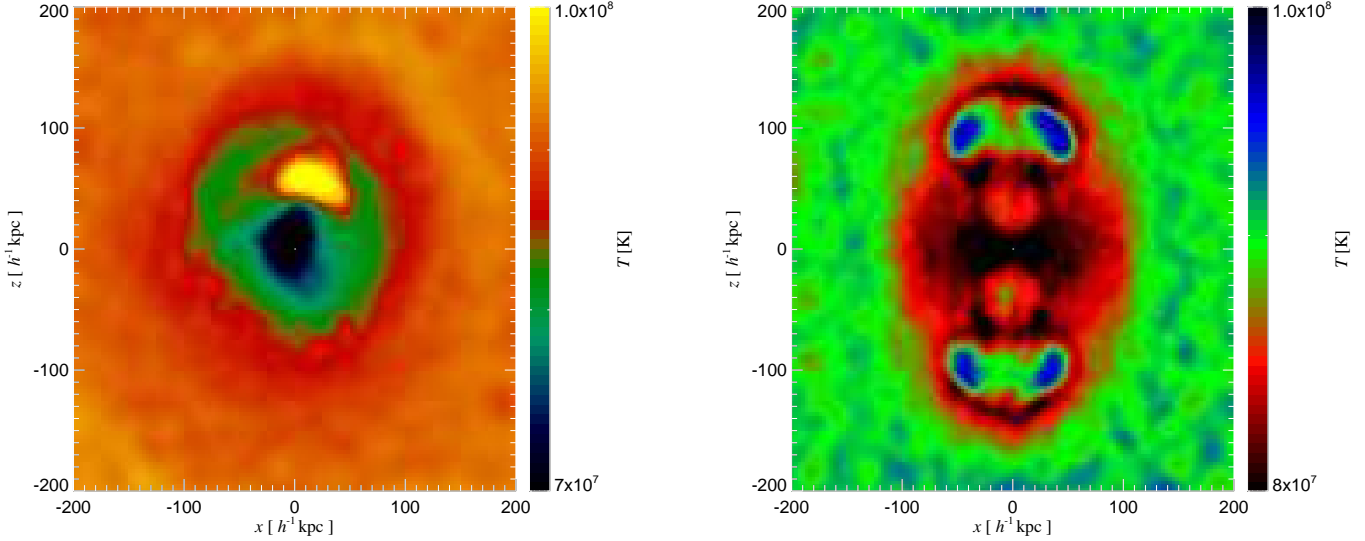


**Figure 1.** Projected mass-weighted temperature maps of the central regions of an isolated galaxy cluster of mass  $10^{15} h^{-1} M_{\odot}$ . In the left panel, bubbles have been introduced with a random placement inside a spherical region, while in the right panel, a “jet-like” injection of bubbles is shown where two bubbles are placed opposite of each other, and subsequent generations of bubbles are injected along the same spatial axis.  $E_{\text{bub}}$ ,  $R_{\text{bub}}$  and  $d_{\text{bub}}$  in both cases are the same, and given by  $5 \times 10^{60}$  erg,  $30 h^{-1}$  kpc and  $50 h^{-1}$  kpc, respectively. The maps have been constructed for times of  $\sim 1.4$  Gyr and  $\sim 0.8$  Gyr after the beginning of the runs.

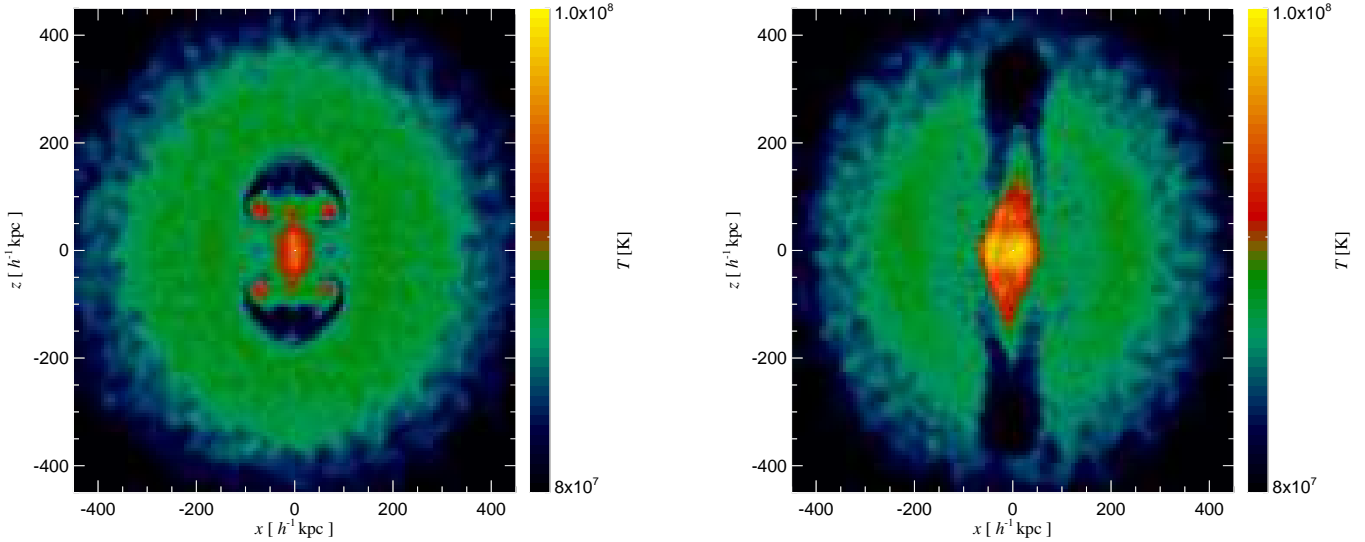


**Figure 2.** Time evolution of the isolated  $10^{15} h^{-1} M_{\odot}$  galaxy cluster with a jet-like AGN heating. The models are the same as in Figure 1, only the bubbles have two times bigger radii, namely  $60 h^{-1}$  kpc. It can be noticed how the morphology in the central cluster region changes due to bubble-induced motions, from  $\sim 1.8$  Gyr (left panel) to  $\sim 3.3$  Gyr, when a well-defined bipolar outflow is clearly visible (right panel).

results with respect to these details of the bubble injection scheme, at least in situations free of secondary effects due to infalling structures and mergers.

In Figure 4, we show unsharped masked maps of the X-ray emissivity of one of our cluster models. The X-ray emission has been estimated using the bremsstrahlung approximation,

$$L_X = 1.2 \times 10^{-24} \frac{1}{\mu^2 m_p^2} \sum_{i=0}^{N_{\text{gas}}} m_{\text{gas},i} \rho_i T_i^{1/2} \quad [\text{erg s}^{-1}]. \quad (7)$$

The unsharp-masking has been performed by subtracting from the original projected  $L_X$ -map the same map smoothed on a  $100 h^{-1}$  kpc scale. A large number of centrally concentrated ripples are clearly visible in the result. These ripples

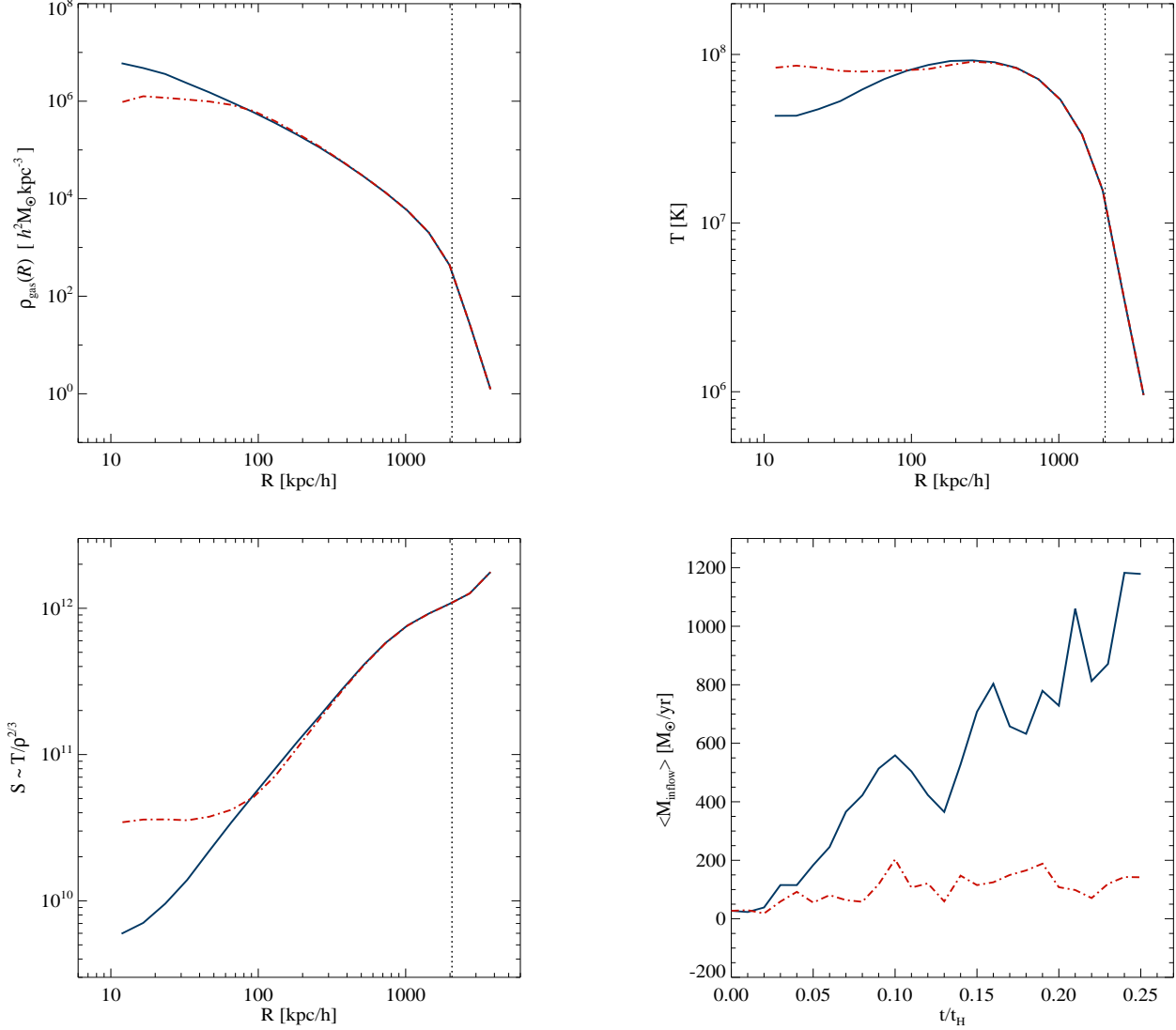


**Figure 3.** Radial profiles of gas density (upper left panel), temperature (upper right panel) and entropy (lower left panel) of the isolated  $10^{15} h^{-1} M_{\odot}$  halo. Blue lines: run with cooling and star formation. Red lines: AGN feedback mechanism also included (random placement of bubbles). The vertical dotted lines denote  $R_{200}$ . Lower right panel: Mean mass inflow rate in the central  $30 h^{-1} \text{kpc}$  as a function of time, normalised to the Hubble time. It can be seen that the mass deposition rate onto the central galaxy is substantially reduced with AGN heating and stabilised at  $\sim 150 M_{\odot} \text{yr}^{-1}$  after a relatively brief period of time.

in the X-ray emissivity are sound waves generated by the expansion of the bubble after the thermal energy is injected. The sound waves travel through the cluster, and if the IGM has a residual viscosity they can be dissipated, providing a nonlocal heating of the central cluster volume. We note that we have explored different scales over which the smoothing in the unsharped masked technique is performed, obtaining the sharpest and most prominent features for smoothing scales corresponding to approximately  $100 h^{-1} \text{kpc}$ , which by order of magnitude agrees with the dimension of the ripples themselves.

We find that the ripples reach distances of  $\sim 800 h^{-1} \text{kpc}$  after 1 Gyr, translating to a velocity of order  $\sim 10^3 \text{ km s}^{-1}$ , which matches the expected sound speed in the ICM of this cluster. At larger radii, the sound waves are not detectable any more. Note that we also expect that their velocity drops

strongly in the outskirts of the cluster, where the temperature and hence the sound speed decline.

Upon closer inspection, it can be seen that the ripples are actually slightly offset from the cluster centre, with their midpoint directly matching the initial coordinates of the injected bubble. Moreover, the ripples progressively lose their intensity at larger radii, both due to a  $1/r^2$  dilution of their intensity, and to a lesser extent, due to a damping caused by the residual viscosity of our SPH scheme. Note that some level of numerical viscosity is intrinsic to all SPH schemes, even though we are modelling an ideal gas. Quantifying the exact magnitude of the resulting effective viscosity is not trivial, also because it depends on the spatial resolution achieved in the simulations. However, recent observations of optical H $\alpha$ -filaments (Fabian et al., 2003b) suggest that the gas in the central region of the cool-core cluster

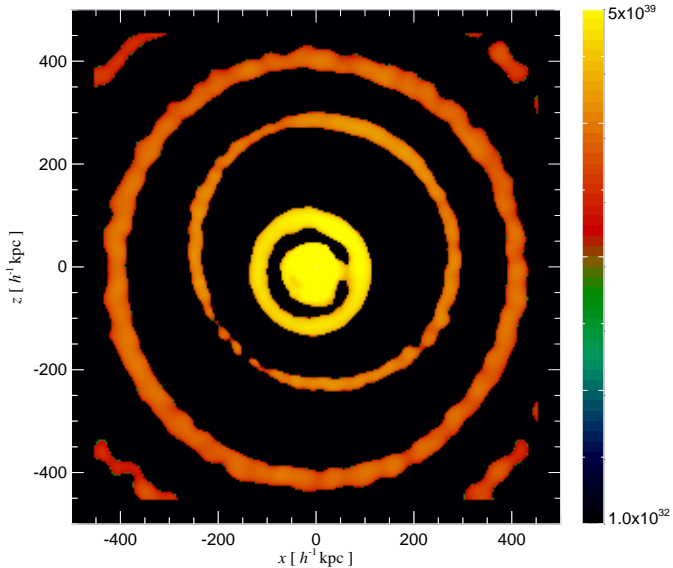


**Figure 4.** Unsharped masked map of the X-ray luminosity in the central region of the  $10^{15} h^{-1} M_{\odot}$  isolated halo, at time  $\sim 2.2$  Gyr. The unsharped masking has been performed by subtracting a smoothed map from the original projected X-ray emissivity map, with the smoothing scale set to  $100 h^{-1} \text{kpc}$ . It can be seen that the AGN bubble heating generates a number of sound waves, which could gradually release their energy to the ICM if they are viscously damped on their way to the cluster outskirts.

Perseus might be quite viscous, rather than turbulent (but see Ensslin & Vogt, 2005, for estimates of gas turbulence on smaller scales). If ICM viscosity is relevant, it would imply a high rate of dissipation of the energy contained in the sound waves at small radii. This physical viscosity could be easily higher than the numerical viscosity we have in our simulations. Naturally, it is then desirable to treat the dissipation process accurately, which requires an SPH discretization of the Navier-Stokes equation combined with an assumed level of physical Spitzer-viscosity. Recently, first mesh-based studies of isolated clusters with viscosity and bubble heating have appeared (e.g. Ruszkowski et al., 2004; Reynolds et al., 2005; Brüggén et al., 2005). We plan to investigate this theoretical issue in a forthcoming study.

In Figure 5, we show the locus of selected particles in the  $\log S - \log R$  plane, at a time equal to one quarter of the Hubble time (which marks the end of most of our isolated simulations). We selected only particles that at least once belonged to one of the injected bubbles. For easier comparison, the mean radial entropy profile of the AGN heated cluster (the same as in Figure 3) is plotted as a red dot-dashed line. The dots shown for each individual bubble particle have been colour-coded according to their relative temperature. The particles of a recently injected bubble have the highest temperature values. As expected, their entropy values lie substantially above the average entropy of the cluster for the same range of radii, implying that the bubble will rise due to buoyancy. We thus expect these bubble particles to

reach larger radii and to lose some of their thermal energy content during the rise, and this expectation is borne out by the cooler particles from older bubbles.

The radius at which the bubble particles attain the mean cluster entropy level is set by their initial density and thermal content after injection, by their capacity to shed some of the energy to the surrounding ICM, by their radiative cooling efficiency, and by the amount of mixing. Given that the different bubbles at various epochs have very similar initial temperature and mass, Figure 5 implies that the bubbles reduce their temperature almost by one order of magnitude, from the injection instant to the final equilibrium position. If we sum up the total energy injected over the entire simulated time, and assume that it gets thermalized over the whole cluster, we obtain that the gas particle temperature is increased by  $\sim 0.2 \text{ keV}$ , which roughly corresponds to the bubble temperature decrement mentioned above when the mass fraction of the bubbles is taken into account. Thus, it appears that the radiative cooling is not severe inside the bubbles, even though in the cluster as a whole it approximately balances the AGN feedback mechanism.

We extended our investigation by considering ‘jet-like’ injection of bubbles and also a scenario in which the bubbles are inflated in a continuous fashion over some time interval  $t_{\text{inj}}$ . We tried values from  $t_{\text{inj}} = 5 \times 10^7 \text{ yrs}$  to  $t_{\text{inj}} = 5 \times 10^8 \text{ yrs}$ , which is significantly longer than the sound crossing time over the scale  $R_{\text{bub}}$  of the bubble. The maximum radius reached by the bubbles is essentially invariant in all of these cases, yielding  $\sim 250 - 300 h^{-1} \text{ kpc}$  at the final simulated epoch. Also, the heating efficiency of buoyant bubbles remains very similar, although the bubbles are somewhat more energetic in the continuous injection scheme, presumably because cooling losses are reduced here due to the expansion of the bubble before the bulk of the energy is released. This is directly reflected in an even lower mass deposition rate onto the central object, which always occurs in a stable fashion with time, where the gas cooling inflow is balanced by the AGN heating rate.

It is important to point out that the entropy content of the bubbles and the maximum distance they can reach from the cluster centre depend upon the equation of state assumed for the gas belonging to the bubbles. In all our models bubbles have been simulated assuming the equation of state of an ideal gas. However, radio observations indicate that AGN-driven bubbles contain relativistic particles which possibly dominate over the thermal pressure component, implying a softer equation of state. Moreover, the energy contrast of the individual bubbles is not very high in our approach, resulting in a gentle ICM heating, without presence of significant shocks. In fact, most of the observations of AGN-heated clusters point out that strong bubble-induced shocks appear to be absent, although recently a few clusters with moderate shocks in connection with AGN activity have been discovered (Fabian et al., 2003a; Nulsen et al., 2005a; McNamara et al., 2005). Therefore, due to the assumptions of our model, the maximum possible distance reached by the buoyant bubbles in the cluster atmosphere may be underestimated with respect to the case where the relativistic particle component is modelled as well.

An important question is whether the bubbles are capable of raising cold gas from the cluster centre and mixing



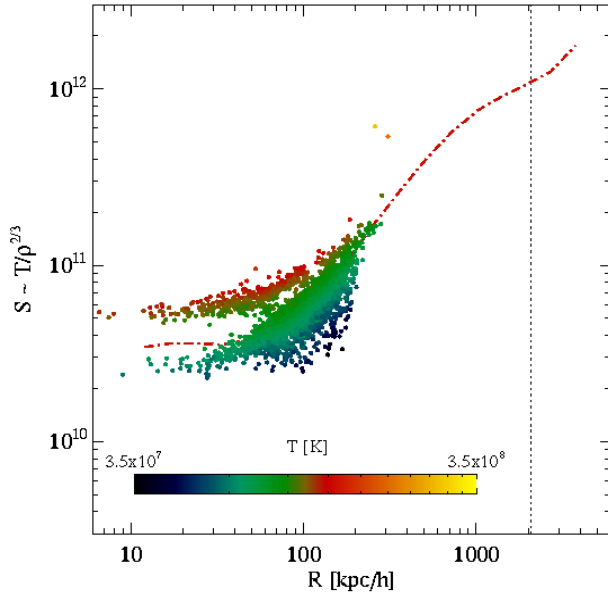


**Figure 5.** Mean radial entropy profile of the  $10^{15} h^{-1} M_{\odot}$  isolated halo. The result for the simulation with AGN feedback is given by the red dot-dashed line. The dots show the positions of the bubble particles, and they are colour-coded according to their temperature.

it with higher entropy gas at larger radii. Note that the X-ray observations of central metal abundance gradients put a constraint on the amount of gas mixing (Böhringer et al., 2004) in the centre. In order to address this issue, we analysed the gas metallicity distribution in the clusters. Without AGN feedback mechanism, all metals produced in the  $10^{15} h^{-1} M_{\odot}$  isolated halo are enclosed in the star forming region and are confined to the very centre, where the density is sufficiently high to allow star formation. The bubble heating instead produces both a reduction of the star formation rate by heating some of the gas that would otherwise end-up in the cold interstellar medium, and a spreading of metals away from the cluster centre. Moreover, in our simple model, the metals produced by the central stars are partly entrained and transported along with the bubbles to larger radii. The spatial distribution of the stars themselves is unaffected by the bubbles, however. It is important to note that the metal mixing in our model due to the bubbles represents a lower limit on the induced additional mixing, because fluid dynamical processes that produce small-scale mixing tend to be underresolved in cosmological simulations.

### 3.2 Efficiency of bubble heating in halos of different mass

The radiative cooling times of halos depend on their mass, both because of their different virial temperatures, and because of the temperature dependence of the cooling rate. Given that the masses of supermassive black holes, and hence our assumed bubble feedback, have a mass dependence as well, we expect a complex interplay between the

different heating and cooling processes, and as a result a mass-dependent efficiency of the feedback. This non-linear dynamics can be best studied with detailed numerical analysis. To this end, we simulated isolated halos for a range of masses, starting from  $10^{12} h^{-1} M_{\odot}$  and reaching up to  $10^{15} h^{-1} M_{\odot}$ , with the characteristics listed in Table 1. The case of the most massive halo has been discussed in some detail in the previous section, so that we can restrict ourselves here to highlight the differences that occur when the mass of the systems is lowered. The study of smaller halos gives also direct insight into the question of how bubble feedback may affect the hierarchical assembly of present-day massive clusters.

In our numerical simulations, the coupled dynamics resulting from cooling, subsequent star formation and a given heating mechanism is quite complex. The introduction of a certain amount of heating can in special situations even trigger an increase of the net cooling rate. For example, let us consider star-forming gas with a density higher than the density threshold set for star formation. If this cold gas component receives an amount of thermal energy from bubble heating that is insufficient to bring it back into the hot phase (where most of the intracluster gas resides), then a counterintuitive process may occur. In this case, the thermal energy injection prevents the cold gas component from forming stars, but the local gas density will remain comparatively high, which in turn stimulates even larger radiative cooling losses. Thus, such a gentle heating, especially in low mass systems where radiative cooling is more pronounced, can in extreme cases even stimulate an increase of the cold gas component.

Analysing diagnostic phase-space diagrams like the  $\log \rho - \log T$  plane, one can notice that for the  $10^{15} h^{-1} M_{\odot}$  halo the relative quantity of central cool gas is low, and it is promptly heated once bubble injection is switched on. Moreover, the energy per bubble particle is sufficiently high to push the gas into the “hot-phase” (upwards and to the left in the diagnostic diagram, as illustrated for the  $10^{14} h^{-1} M_{\odot}$  halo in Figure 6) and the star formation at late simulated epochs is completely quenched.

Examining the  $10^{14} h^{-1} M_{\odot}$  isolated halo, we find that bubbles are still very efficient in reducing the star formation rate, e.g. after the time  $t_H/4$ , only 14% of stars are formed with respect to the run without AGN heating, but the total amount of cold gas, both in the central regions and out to  $R_{200}$ , remains very similar. The diagnostic diagram for this cluster is shown in Figure 6. The small orange dots are the gas particles for the run without AGN feedback, and they maintain practically the same position even when bubble heating is included. The big blue dots are those gas particles that belong to the ‘cold phase’, here defined as having temperatures less than 1 keV and densities higher than the density threshold set for star formation (as indicated by the vertical dotted line). With AGN heating included, the red dots denote the bubble particles, while the green star symbols give the locations of cold phase gas particles. Two different features due to the presence of bubble feedback are readily apparent. First, the cold gas fraction for the intermediate temperature range, from  $5 \times 10^5$  K to  $10^7$  K, is substantially reduced in the case with feedback, because for most of these particles it is possible to transport them back to the hot phase. In contrast, along the line in the lower-right part of

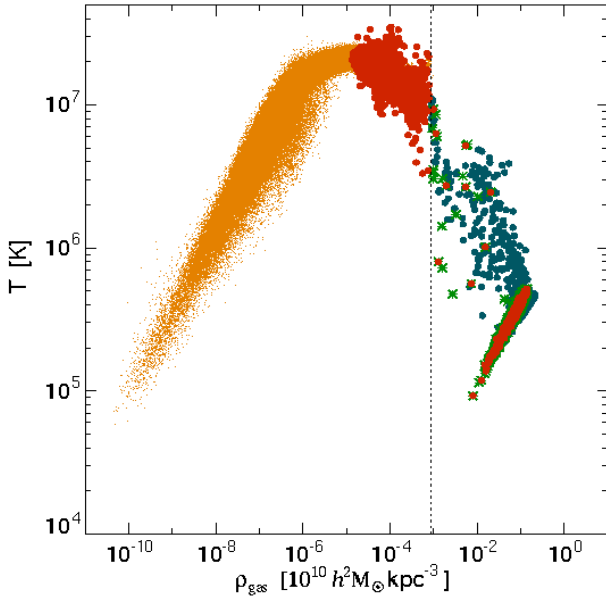


**Figure 6.** Phase-space diagram of gas temperature versus gas density for the  $10^{14} h^{-1} M_{\odot}$  galaxy cluster. Small orange dots are the particles outside the cold star-forming region, while big blue dots denote the gas particles in the run with no feedback, at high overdensities and with temperatures below 1 keV. Green star symbols are the particles satisfying the same criteria, but when the AGN heating is included. Finally, the position of the bubble particles is given by red dots.

the diagram, there are more particles when bubble heating is included. This can be explained by the fact that this line is determined by the multiphase structure of the ISM, given here in terms of an effective mass-weighted mean temperature, which is a combination of the temperature of cold gas clouds and the one of the hot ISM component (see Springel & Hernquist, 2003). Hence, while the feedback mechanism reduces the number of stars formed, it produces a higher amount of interstellar gas with very low temperatures. Note that a large fraction of these cold gas particles have been a part of a bubble at some earlier epoch.

In the lower mass system of mass  $10^{13} h^{-1} M_{\odot}$ , the final number of stars is also reduced, this time by only 13%, and, as well as in the previous case, the cold gas fraction is essentially unchanged. In the most extreme case of the  $10^{12} h^{-1} M_{\odot}$  halo, the bubble heating of the ICM is radiated away on a very short timescale without producing any substantial modification.

We considered different injection assumptions in order to test whether this effect can be alleviated and the bubble heating efficiency can be increased. Focusing on the most difficult case of the  $10^{12} h^{-1} M_{\odot}$  halo, we explored a range of injection energies, from  $5 \times 10^{56}$  erg per bubble, to  $3 \times 10^{57}$  erg. Also, we injected bubbles according to different schemes: in a spatially correlated ‘jet-like’ fashion, or by inflating the bubbles gradually for  $t_{\text{inj}} = 5 \times 10^7$  yrs, i.e. by releasing the energy slowly instead of instantaneously. Finally, we also tried a model where we artificially prevented bubble particles from cooling for  $10^7 - 10^8$  yrs, motivated by some observational ev-

idences that the bubbles contain a non-thermal component, which would then be able to maintain its pressure longer. From these experiments we conclude that relating the bubble energetics to the underlying dark matter potential by invoking an assumed relation with its black hole mass, does not in general provide stable solutions for an efficient elimination of cooling flows in low mass systems. Unrealistically high bubble energies are required in order to offset the cooling flow, and also their thermal content has to be fine-tuned to a restricted range of values, otherwise AGN heating may easily become so strong that bubbles blow out substantial amounts of mass from the halo or cluster potential well.

This clearly indicates an important deficiency of bubble models like the one studied here. Since there is no internal trigger for bubble activity, a self-regulation loop is missing, but this will be required for stability in more general situations. Therefore, a more detailed physical scenario for the triggering of bubble activity is needed which couples the local physics of the cooling flow with the activity and energetics of AGN feedback. We will discuss a number of possibilities for this in Section 5.

### 3.3 Observational X-ray features of simulated bubbles

In the last few years, a growing number of observations performed with the Chandra X-ray telescope have found the presence of so called X-ray cavities in central galaxy cluster regions (e.g. McNamara et al., 2000; Fabian et al., 2000; Sanders & Fabian, 2002; Mazzotta et al., 2002; Birzan et al., 2004). These observations support a scenario where relaxed cooling-flow/cooling-core clusters are heated due to the presence of a supermassive black hole at their centres. Hence, it is interesting to see whether the simulated bubbles produced by our model have morphologies comparable to the observed ones.

In order to perform this comparison accurately, it is necessary to produce artificial emissivity maps which are as similar as possible to realistic observations based on a finite exposure time on an X-ray telescope. Recently, a similar analysis has also been performed by Brüggén et al. (2005). To this end, we processed selected simulation outputs with the X-MAS software package. A final result of this code is a photon event file quite similar to the one an observer would acquire with the Chandra telescope in ACIS-S3 mode. The instrument background has been included in our images by taking into account an appropriate blank-sky background file (Markevitch et al., 2001). A detailed description of the X-MAS simulator can be found elsewhere (e.g. Gardini et al., 2004); here we limit the description to the subsequent analysis steps performed and the significance of the maps obtained.

We have generated event files for different exposure times, ranging from 10 ks to 1 Ms, both for the runs with and without AGN feedback. We then selected a number of different energy bands, performed a Gaussian smoothing on a range of scales, and finally produced unsharp masked images to search for evidence of systematic departures of the flux from the mean. In Figure 7, we show photon images of

the central region of the  $10^{15} h^{-1} M_{\odot}$  isolated halo<sup>†</sup>, both in a case with and without additional AGN heating. The physical scale of the maps corresponds to  $\sim 670$  kpc (2048pix), the energy band has been chosen to be  $\Delta E = [0.3, 1.5]$  keV, and the maps have been smoothed by summing the pixel fluxes in bins of 4 pixels. For this  $\Delta E$ , the instrument background is minimised and the features due to the presence of the bubbles are more evident.

The first panel of Figure 7 shows a photon image of the AGN-heated cluster after 100 ks of exposure time, before applying any smoothing. The rest of the plots have been created by Gaussian smoothing them first on a small scale (3pix), then re-smoothing the obtained image on a bigger scale (15pix), and finally unsharp masking the two smoothed images (i.e. subtracting off the 15pix smoothed version). The smoothing scales have been selected to maximise flux departures from the mean. The second and the third panel illustrate how the bubbles introduce emissivity irregularities for two different exposure times, 100 ks and 1 Ms, respectively. Finally, the fourth panel presents the cluster photon image after an exposure time of 100 ks and with no AGN feedback.

It is clear that the bubbles generate characteristic fluctuations in the photon counts, both creating bright features and X-ray depressions. The typical dimension of these irregularities is  $\sim 50$  kpc, very similar to the size of the bubbles themselves. The hot spots can be associated with the most recent bubble events, containing particles still significantly hotter than the surrounding ICM (as can be also seen from Figure 5), whereas the depressions in photon counts can be explained with previous bubble episodes. These peculiarities in emissivity are completely absent in the galaxy cluster without AGN feedback, indicating that they are real features and not artifacts produced by counting statistics or our analysis. The only feature that is present in the fourth panel of Figure 7 is the central excess due to the prominent cooling flow of  $\sim 100$  kpc size in diameter. Based on these results we conclude that in a relaxed galaxy cluster, departures from the mean flux stemming from bubbles with characteristics as given by our model can be detected, provided the exposure times are long enough, and provided that other sources of photon count deviations are absent or negligible.

## 4 EFFECT OF AGN BUBBLE HEATING IN COSMOLOGICAL SIMULATIONS

### 4.1 Simulation characteristics

As a next step in our analysis, we consider the importance of AGN feedback in full cosmological simulations of cluster formation. To this end, we selected a number of galaxy clusters with a wide range of masses from a parent dark matter simulation, and resimulated them with higher resolution including gas dynamics. Our hydrodynamical simulations account for cooling and star formation, and additional AGN heating as well. In a subset of our runs, we also included

galactic winds powered by star formation, as implemented by Springel & Hernquist (2003). Models with winds provide a better description of some galaxy cluster properties, e.g. the distribution of metals, but in order to be able to cleanly identify the effects of bubble heating, we focus most of our analysis on simulations without winds. Where appropriate, we will however briefly discuss any changes of our results when winds are also included.

Our primary series of simulations consist of resimulations of a cluster extracted from the GIF  $\Lambda$ CDM simulation (Kauffmann et al., 1999). We selected the second most massive galaxy cluster from this simulation and constructed higher resolution initial conditions for it using the “Zoomed Initial Conditions” technique (Tormen et al., 1997). We carried out two runs with different resolution in order to test numerical convergence of our results. These clusters are equivalent to the ones used by Springel et al. (2001a), but with gas (from now on we will refer to these runs as S1 and S2, respectively). The simulations have been evolved from an initial redshift of  $z_{\text{ini}} = 30$  for S1, and  $z_{\text{ini}} = 50$  for S2, producing 25 outputs uniformly spaced in the logarithm of the expansion factor. Additionally, we selected two other clusters with final virial masses substantially smaller (g676) and bigger (g1) than the S1/S2-cluster. These clusters have been extracted from a cosmological  $\Lambda$ CDM simulation of box-size  $479 h^{-1} \text{Mpc}$  (Yoshida et al., 2001; Jenkins et al., 2001), and again have been resimulated with the ZIC technique at higher resolution (Dolag, 2004).

The simulation of the g1 galaxy cluster includes several other smaller systems in the high-resolution region which we also included in our analysis. Tables 2 and 3 provide a summary of the main properties of our set of simulated galaxy clusters. In all runs, the cosmological parameters were that of a flat concordance  $\Lambda$ CDM model, with  $\Omega_m = 0.3$ ,  $\Omega_{\Lambda} = 0.7$ ,  $\Omega_b = 0.04$ , a normalisation of the power spectrum given by  $\sigma_8 = 0.9$ , and a Hubble constant at the present epoch of  $H = 70 \text{ km s}^{-1} \text{ Mpc}^{-1}$ .

Unlike simulations of isolated clusters, cosmological simulations require a special algorithmic method for placing bubbles, since the position of the cluster centre and properties like virial mass are not known a priori, and change with time. To address this problem, we run for every AGN duty cycle a fast parallel FOF group finder on the fly as a part of the simulation code, obtaining a list of all halos with their basic properties. We then adopt two different schemes for injecting bubbles. We either consider only the most massive halo found in the high-resolution zone, which can be identified with the most massive progenitor of the final cluster, or we introduce AGN-driven bubbles in all halos above a given fixed mass threshold value. The injection of bubbles in all large halos is motivated by the observational indications that probably most if not all of the spheroidal galaxies harbour a supermassive black hole at their centres. Note that the larger number of bubbles in this second scenario can also cause additional effects during merger events, where bubble material can be torn apart and mixed into outer regions of the cluster.

<sup>†</sup> We decided to perform this analysis on an isolated cluster in order to minimise other features in the X-ray emissivity that would have been imprinted by possible substructures or merger events. Further discussion of this issue in the cosmological framework is given in Section 4.5.

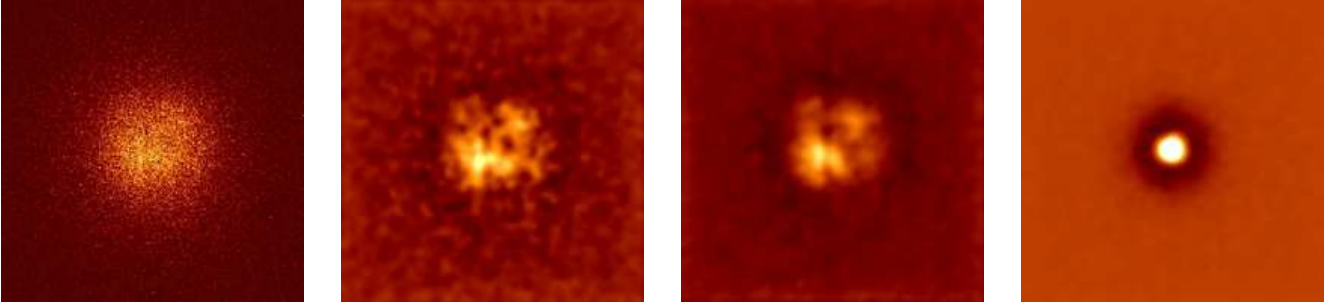


**Figure 7.** Artificial photon images for the  $10^{15} h^{-1} M_{\odot}$  isolated galaxy cluster obtained with the X-MAS software package. In all the panels, photons have been selected in the energy band  $\Delta E = [0.3, 1.5]$  keV, maps were binned in 4pix/bin, and the physical scale of the maps is  $\sim 670$  kpc. The cluster emissivity map before applying any smoothing is illustrated in the first panel, while all the other panels have been obtained by unsharp masking previously smoothed images, as explained in the text. The second and the third panels show qualitatively very similar features. They are for the run with AGN feedback and differ only in the exposure time. Finally, the fourth panel shows how the same cluster appears when the bubble heating is absent.

| Simulation | $N_{\text{HR}}$ | $N_{\text{gas}}$ | $m_{\text{DM}} [h^{-1} M_{\odot}]$ | $m_{\text{gas}} [h^{-1} M_{\odot}]$ | $z_{\text{start}}$ | $z_{\text{end}}$ | $\epsilon [h^{-1} \text{kpc}]$ |
|------------|-----------------|------------------|------------------------------------|-------------------------------------|--------------------|------------------|--------------------------------|
| S1         | 450088          | 450088           | $5.96 \times 10^9$                 | $0.92 \times 10^9$                  | 30                 | 0                | 14.5                           |
| S2         | 1999978         | 1999978          | $1.18 \times 10^9$                 | $0.18 \times 10^9$                  | 50                 | 0                | 8.5                            |
| g676       | 314518          | 314518           | $1.13 \times 10^9$                 | $0.17 \times 10^9$                  | 60                 | 0                | 5.0                            |
| g1         | 4937886         | 4937886          | $1.13 \times 10^9$                 | $0.17 \times 10^9$                  | 60                 | 0                | 5.0                            |

**Table 2.** Numerical parameters of the cosmological galaxy cluster simulations used in this study. The values listed from the second to the fifth column refer to the number and to the mass of high resolution dark matter particles and of gas particles. Note that the actual values of  $N_{\text{gas}}$  and  $m_{\text{gas}}$  vary in time due to star formation. The last three columns give the initial and final redshifts of the runs, and the gravitational softening length  $\epsilon$ .

#### 4.2 Global gas properties of simulated galaxy clusters

Before analysing the properties of simulated galaxy clusters with and without AGN bubble heating, we briefly discuss issues of numerical convergence. For this purpose we consider the S1 and S2 runs, and compare their spherically averaged radial profiles at two epochs, namely at  $z = 3$  and  $z = 0^{\ddagger}$ . The dark matter and stellar density profiles of the S1 and S2 galaxy clusters are in excellent agreement at both epochs, as well as the gas density profiles, with the residual differences at early times being consistent with what is expected from the increased noise. Both the emission-weighted and the mass-weighted temperature profiles do not noticeably differ at low redshifts, while there is a hint of a slightly higher gas temperature for the S2 cluster at early times. Thus, we conclude that for radii larger than the gravitational softening length the properties of our simulated galaxy clusters are numerically robust and have converged quite well.

In Figure 8, we compare the gas entropy profiles with and without bubble heating at three different epochs,  $z = 1.64$ ,  $z = 0.44$  and  $z = 0$ . For this comparison, we use both of our AGN heating models, the one based on the Magorrian relationship and the “BHAR model”. The entropy has been estimated by calculating the ratio of the emission-weighted temperature to the gas density elevated to the  $2/3$  power,

<sup>‡</sup> These two epochs delimit the time interval during which the bubble heating is active, and hence the period of time where our analysis is performed.

where the temperature is measured in Kelvin and the gas density is given in  $h^2 M_{\odot} \text{kpc}^{-3}$ . We selected only the hot gas component to compute these profiles, i.e. we avoided the cold, star-forming gas by imposing a cut in density and ionisation level. With this choice, the gas profiles are smoother because they have no contributions from cool substructures at various radii. Nonetheless, it is also important to investigate the fate of the cold gas in the central cluster region, an issue we will address separately in Section 4.3. The blue continuous lines are for the run without AGN feedback, the red dot-dashed lines correspond to the “Magorrian model”, while the green dashed lines are for the “BHAR model”. The vertical dotted lines denote the softening length and the virial radius at the different epochs, respectively. When  $E_{\text{bub}}$  is computed from the “BHAR model”, the effect of bubbles is less prominent at low redshifts than in our other AGN heating scenario. However, at early times the situation is opposite, as expected. Here the “BHAR model” heats the ICM gas more prominently, right from the initial injection epoch ( $z = 3$ ) until  $z \sim 0.4$ . It is interesting to note that at  $z \sim 0.4$  the bubble energy content is already much lower than in the “Magorrian model”, indicating that the efficient heating at early times has a prolonged effect on the thermodynamic state of the galaxy cluster. We find that the “Magorrian model” starts to affect the gas entropy from  $z \approx 1.6$  in a noticeable way and it becomes very important at late times, where it suppresses the cooling flow completely at  $z = 0$ . As a further comparison, we show in Figure 9 radial profiles of gas density, temperature, X-ray luminosity, and local cooling time for the S1 galaxy cluster at  $z = 0$ .

| Cluster | $R_{200}$ [ $h^{-1}\text{kpc}$ ] | $M_{200}$ [ $h^{-1}M_{\odot}$ ] | $T_{\text{mw}}$ [K] | $T_{\text{ew}}$ [K] | $L_{\text{X}}$ [ $\text{ergs}^{-1}$ ] |
|---------|----------------------------------|---------------------------------|---------------------|---------------------|---------------------------------------|
| S1      | 2427                             | $9.98 \times 10^{14}$           | $5.2 \times 10^7$   | $8.7 \times 10^7$   | $9.8 \times 10^{44}$                  |
| S2      | 2466                             | $1.05 \times 10^{15}$           | $5.1 \times 10^7$   | $8.8 \times 10^7$   | $9.9 \times 10^{44}$                  |
| g676    | 1176                             | $1.13 \times 10^{14}$           | $1.4 \times 10^7$   | $2.6 \times 10^7$   | $1.6 \times 10^{43}$                  |
| g1_a    | 2857                             | $1.63 \times 10^{15}$           | $7.3 \times 10^7$   | $1.3 \times 10^8$   | $1.0 \times 10^{45}$                  |
| g1_b    | 1914                             | $4.89 \times 10^{14}$           | $3.1 \times 10^7$   | $4.1 \times 10^7$   | $1.2 \times 10^{44}$                  |
| g1_c    | 1448                             | $2.12 \times 10^{14}$           | $1.5 \times 10^7$   | $2.5 \times 10^7$   | $3.0 \times 10^{43}$                  |
| g1_d    | 1258                             | $1.39 \times 10^{14}$           | $1.6 \times 10^7$   | $1.9 \times 10^7$   | $1.8 \times 10^{43}$                  |
| g1_e    | 1085                             | $8.92 \times 10^{13}$           | $1.1 \times 10^7$   | $1.6 \times 10^7$   | $7.0 \times 10^{42}$                  |

**Table 3.** Physical properties of our sample of simulated galaxy clusters at  $z = 0$  and at  $200\rho_c$ . For different galaxy clusters, labeled in the first column, cluster radius, total mass, mass- and emission-weighted gas temperature and X-ray luminosity are listed, respectively. Note that the values refer to the simulations with cooling and star formation, without bubble heating included.

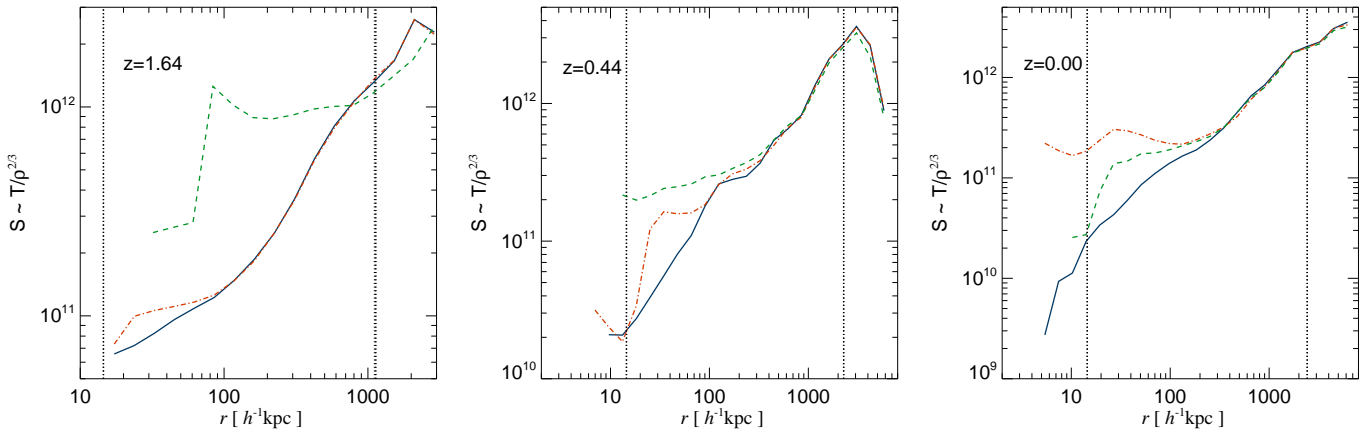


**Figure 8.** Radial profiles of gas entropy of the S1 galaxy cluster simulation. The blue continuous lines are for the run with cooling and star formation only, the red dot-dashed lines refer to the case when AGN heating based on our “Magorrian-like scheme” is included as well, while the green dashed lines are for the BHAR-based model. The dotted vertical lines denote the gravitational softening and the virial radius at the given redshift; the latter is indicated in the upper-left corner. The profiles do not extend down to vanishingly small radii because they have been calculated exclusively from the hot gas component (basically the gas above 1 keV), excluding the cold dense gas in the centre. Note that both the spatial and the entropy scale vary between the three different panels.

AGN heating alters the gas properties out to a radius of  $\approx 300 h^{-1}\text{kpc}$ , reducing the central gas density and increasing its temperature. The X-ray emissivity, being more sensitive to the gas density, is substantially lower when bubble feedback is active. In the lower-right panel of Figure 9, we show the cooling time of all ICM gas, estimated isobarically as (Sarazin, 1988)

$$t_{\text{cool}} = 8.5 \times 10^{10} \left( \frac{n_p}{10^{-3} \text{cm}^{-3}} \right)^{-1} \left( \frac{T}{10^8 \text{K}} \right)^{1/2} \text{ [yrs]}, \quad (8)$$

where  $n_p$  is the number density of hydrogen. When AGN heating is not included, the cooling radius, i.e. the radius where  $t_{\text{cool}} = t_{\text{H}}$ , lies at  $\sim 60 h^{-1}\text{kpc}$ , while it gets reduced to  $\sim 25 h^{-1}\text{kpc}$  in our “BHAR model”. However, the cooling radius vanishes for the “Magorrian model”, where the bubbles injection heats the gas above 1 keV.

Even though the spatial extent of the bubble particles reaches out to the virial radius of the cluster, they are not capable of heating the gas in outer regions, simply because their entropy content becomes comparable to the entropy of the surrounding ICM gas at intermediate radii. This finding is analogous to the previously discussed case of isolated

halos, but the dynamical evolution of the cluster with its associated merger processes makes spreading of bubble material towards the outskirts more efficient.

In Figure 10, we show emission-weighted temperature maps of the g676 galaxy cluster at four different epochs, in order to more closely discuss the spatial distribution of bubbles during merger events. The over-plotted dots represent the particles that at least once belonged to a bubble, and they are colour-coded according to their temperature, the darkest ones are particles with  $T > 10^8 \text{K}$ , while the lightest have  $T < 10^4 \text{K}$ . For this analysis, we have introduced AGN feedback in all halos above  $5 \times 10^{10} h^{-1}M_{\odot}$  and we scaled the energy content of the bubbles with  $M_{200}^{4/3}(z)$  of the host galaxy cluster.

In the first panel at redshift  $z = 0.86$ , there is a smaller halo on the lower right corner which enters the most massive cluster progenitor at that epoch (which roughly has three times larger mass), which is located at the centre of the panel. Both the massive halo and the smaller one are AGN heated, but the bubbles are less energetic for the infalling halo due to our assumed mass dependence. Moreover, it can be noticed that the bubbles occupying the central regions

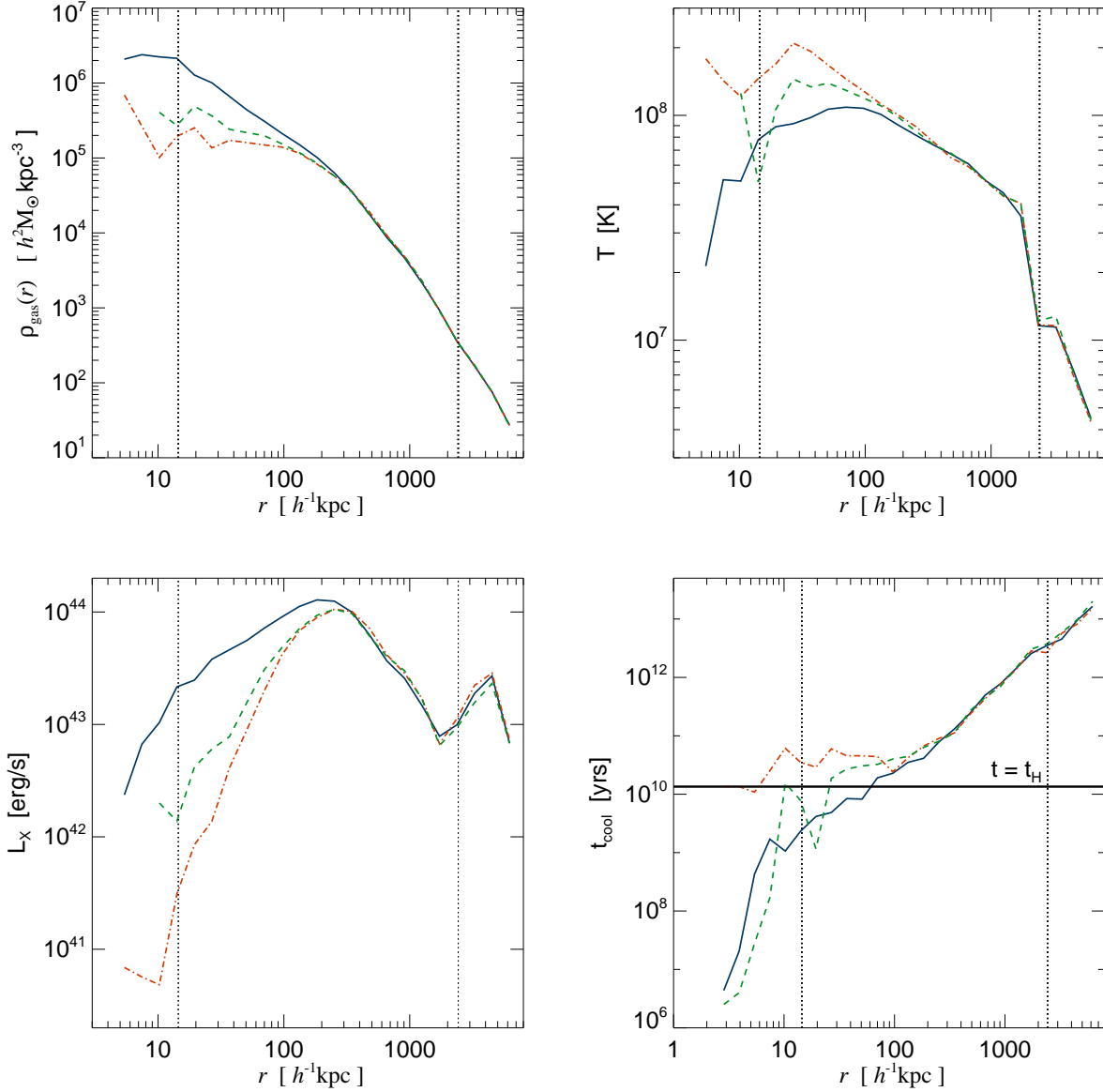


**Figure 9.** Radial profiles at  $z = 0$  of gas density (upper-left panel), emission-weighted temperature (upper-right panel), and X-ray luminosity (lower-left panel) estimated with the bremsstrahlung approximation given by eq. (7). The lower-right panel shows the cooling time of all gas particles as a function of radius, computed using eq. (8). The continuous horizontal line indicates the Hubble time at  $z = 0$ . The blue continuous lines are for the case without AGN feedback, the red dot-dashed lines are for the model where  $E_{\text{bub}} \propto M_{200}^{4/3}(z)$ , while the green dashed lines are for the scenario where the bubble energy depends on the BHAR given by eq. (3).

are hotter, both because they are more recent and thus have had less time to lose their energy content, and also because at later times bubbles are intrinsically more energetic in our “Magorrian scenario”. The second panel of Figure 10 (at  $z = 0.62$ ) illustrates what happens to the bubble distribution when the smaller halo is crossing the central region of the massive cluster. The bubbles are literally pushed out of the way, upwards and to the right, and they are also heated. The next panel (at  $z = 0.48$ ) shows that the bubble distribution is still quite asymmetric, but at the same time, bubbles have spread efficiently into outer regions and also have cooled. Finally, the last panel shows how the cluster

appears at  $z = 0.20$ , where it starts to be fairly relaxed with a quite symmetric distribution of bubbles.

### 4.3 Stellar properties of galaxy clusters

In this section, we analyse the effects of AGN heating on the properties of the stellar components of galaxy clusters. We concentrate on the properties of the central cluster galaxy, which is the one affected most by the bubble heating. From the initial injection epoch ( $z = 3$ ) until  $z = 0$ , we compute for this purpose the stellar and gaseous mass, star formation rates, stellar ages, and colours of the cD galaxy that sits in the main progenitor of our final halo.

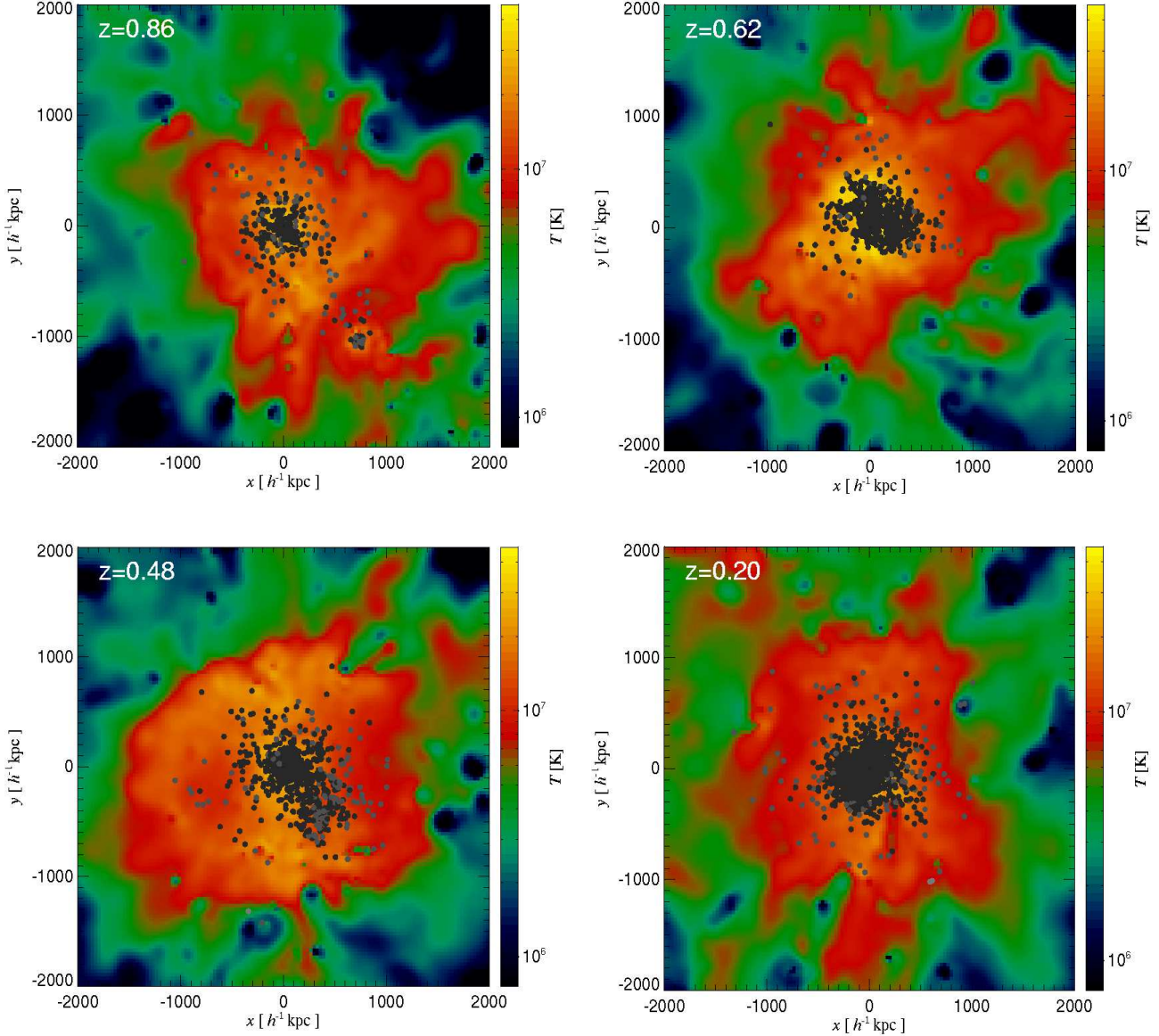


**Figure 10.** Emission-weighted temperature maps of the g676 galaxy cluster simulation during a major merger event at  $z = 0.86, 0.62, 0.48$  and  $0.20$ , respectively. Over-plotted dots represent gas particles that have been at least once part of a bubble, and they are colour-coded according to their temperature, the darkest ones being the hottest. It can be noticed that both the spatial distribution of bubbles and their energy content are drastically influenced by the passage of the smaller halo through the central region of the massive cluster.

In Figure 11, we show a histogram of the formation times of stars belonging to the cD galaxy at  $z = 0$  of our S1 galaxy cluster. The histograms have been computed by binning the expansion factors that correspond to each stellar formation time, and they have been normalised to the maximum bin. The white histogram is for the run without AGN heating, the grey coloured one for the “Magorrian model”, while the hatched histogram gives the result for “BHAR model”. When AGN heating is absent, the histogram of stellar formation redshifts clearly shows an extended tail at low redshifts; together with the considerable SFR of order of  $100 M_{\odot} \text{yr}^{-1}$ , this implies that stars are formed until  $z = 0$  in situ. Nevertheless, there is a possibility that some of these stars have been formed elsewhere, e.g. in merging substruc-

tures, and that they only ended up later in the cD galaxy by merging. For redshifts less than 0.3 this is certainly not an important mechanism, because in our “Magorrian model”, the central SFR is completely suppressed for  $z < 0.3$  and at the same time the  $z_{\text{sf}}$  histogram is truncated. Thus, the difference of  $\sim 6 \times 10^{11} h^{-1} M_{\odot}$  in the stellar mass of the final cD galaxy in these two cases gives an indication on how many stars have formed in the cD galaxy from  $z = 0.3$  until today, when AGN feedback is not present. At the same time, also the mass of the cold gas (below 1 keV) is reduced in the “Magorrian model”, from  $\sim 2 \times 10^{10} h^{-1} M_{\odot}$  to zero. Moreover, the suppression of star formation at late times has an immediate effect on colours of the cD galaxy, which becomes redder. To estimate the colours we used Bruzual

& Charlot’s stellar population synthesis models (Bruzual & Charlot, 2003), computing rest-frame magnitudes in the SDSS bands, assuming Solar metallicity and a Chabrier initial mass function. The  $u$ -band magnitude is changed from  $-23.8$  to  $-22.8$  and the  $u-r$  colour is increased from 2.0 to 2.6.

In contrast, the star formation of the “BHAR model” proceeds in a quite different manner, as can be seen from the hatched histogram, which is substantially lower for  $0.4 < z < 2.0$ , but quite similar to the case without AGN feedback at very low redshifts,  $z < 0.3$ . The first feature arises due to two different processes happening at the same time. The second peak present in the histograms is due to a major merger event that happens roughly at  $z = 1$ . One consequence of this merger event is a central burst of star formation, which happens to be absent in the “BHAR model” due to its very efficient bubble heating at this epoch. Nonetheless, there are still some stars becoming part of the cD galaxy at  $z = 0$  that have formation times in the corresponding time interval. Tracing back these stars in time and considering that the SFR of the cD galaxy in the “BHAR model” during this epoch is practically zero, we see that these stars have been produced in other small galaxies and were indeed accreted onto the central cD galaxy at later times. Assuming that a similar amount of stars accreted onto the cD galaxy also in the case without AGN feedback, a total mass of  $\sim 10^{12} h^{-1} M_{\odot}$  in stars has formed in situ between  $z = 2$  and  $z = 0.4$ , with a considerable part created as part of the central starburst induced by the major merger event.

The tail at low redshifts present in the hatched histogram can be explained by the reduced energy content of the bubbles, which are not efficient any more in suppressing the cooling flow, and consequently the star formation in the central cD galaxy. The total SFR within  $R_{200}$  follows a similar trend as the SFR of the cD galaxy, with comparable systematic differences for the different runs, implying that the bubble heating mainly affects the central stellar properties and not the residual star formation in the cluster volume.

#### 4.4 The metallicity distribution in the simulated clusters

In this section, we analyse the metal distribution in our simulated galaxy clusters. It is a well known problem that numerical simulations which include cooling and star formation processes in general fail to reproduce the observed shallow metallicity gradients, especially so if efficient feedback mechanisms that help spreading the metals are absent. In particular, metals produced by stars remain locked in the dense, star forming regions, even though supernovae feedback is included which regulates the star formation process itself. As a result, the metallicity distribution remains lumpy and exhibits a rather step gradient. Moreover, most of the metals are produced in the central cD galaxy due to its excessive star formation, which is a manifestation of the cooling flow problem.

This motivates the search for physical feedback processes that can spread and mix metals more efficiently, acting both in the central region and on the scale of the whole galaxy cluster. While the galactic wind model suggested by

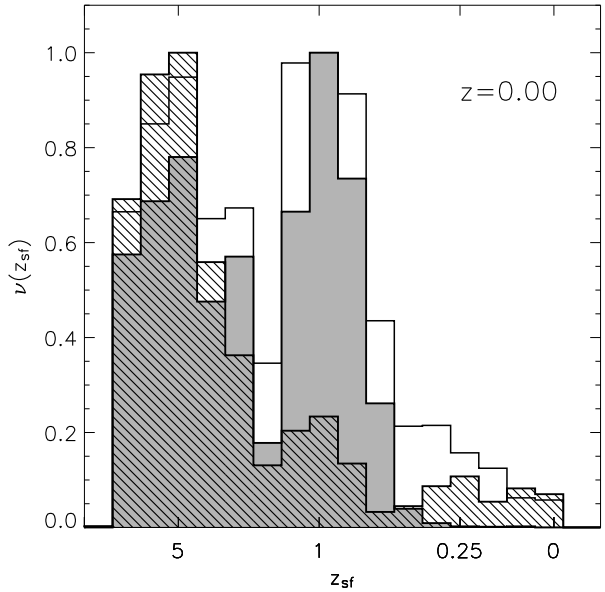


**Figure 11.** Distribution of formation redshifts of the stars belonging to the cD galaxy of the S1 galaxy cluster at  $z = 0$ . The white histogram corresponds to the case with cooling and star formation only; here it can be seen that stars continue to be formed until  $z = 0$ . The grey coloured histogram shows how the stellar formation times change when our “Magorrian model” of bubble heating is switched on, which essentially suppresses any central star formation for  $z < 0.25$  completely. Finally, the result for the “BHAR model” of AGN feedback is illustrated with the hatched histogram, which shows a considerable suppression of central star formation at intermediate redshifts,  $0.3 < z < 2.0$ .

Springel & Hernquist (2003) helps in reducing this discrepancy and also diminishes the total SFR over cosmological time, the model fails to qualitatively change the gas and stellar properties of galaxy clusters discussed in Sections 4.2 and 4.3. Especially at late times, mixing of metals due to winds from the cD galaxy proves inefficient; here the cluster potential well is simply too deep and the ram pressure of the ICM too high to allow winds to travel far. Bubble heating may fare considerably better in this respect. In the following we therefore analyse the effect of AGN on the metal distribution in our simulations, and we also compare simulations with or without galactic winds of velocity  $\sim 480 \text{ km s}^{-1}$ .

In Figure 12, we show radial profiles of the gas metallicity of the S1 galaxy cluster, and in Figure 13 we illustrate the corresponding mass-weighted gas metallicity maps. When additional feedback mechanisms are taken into account, the amount of metals in the hot gas component is increased with respect to runs with cooling and star formation only (continuous blue line on Figure 12 and left panel of Figure 13). Also, the metallicity distribution becomes less lumpy because the metals are more efficiently transported out of the dense regions, increasing the fraction of enriched gas. It can be noticed that already bubble heating without winds (red dot-dashed line in Figure 12, and middle panel of Figure 13) is capable of producing a more homogeneous metallicity distribution, while the AGN heating coupled with the galactic



winds (green dashed line in Figure 12 and right panel of Figure 13) slightly decreases the radial metallicity gradient and makes the spreading of the metals even more efficient.

Nevertheless, the total amount of metals in the three different ICM phases – hot ICM gas, cold star-forming gas, and stars – remains very similar in all runs, implying that there are no substantial metal-enriched gas outflows from the galaxy cluster itself. The situation can be rather different if winds with similar velocities are present in less massive systems, as demonstrated by Springel & Hernquist (2003). When the galactic wind velocities become comparable to the escape velocity from the system in consideration, then the winds may lead to gaseous outflows, eventually polluting the surrounding medium with metals produced by cluster stars. The heating provided by bubbles might help the metal spreading even more. Considering our “BHAR model” at early times where it is very efficient and when the corresponding halo mass is considerably smaller, there is evidence that not only many metals are transferred into the “hot phase”, but also that metal enriched gas is pushed towards the cluster outskirts, and in part beyond the virial radius. However, this effect is transitory, because  $E_{\text{bub}}$  decreases with time, and more importantly, because the forming cluster is so massive that it behaves effectively like a closed box at late times. Consequently, at  $z = 0$ , the distribution of metals looks quite similar to the “Magorrian model” discussed above. Finally, note that even though bubble heating improves metal spreading in the ICM, at the same time it does not disrupt the central metallicity gradient of the galaxy clusters, as can be clearly seen from Figure 12. Therefore, our AGN heating prescription is qualitatively in good agreement with the metallicity gradients observed in cool core clusters (e.g. Böhringer et al., 2002; De Grandi et al., 2004; Böhringer et al., 2004).

#### 4.5 Sound waves or merger induced weak shocks?

While the unsharp mask technique is very useful in detecting X-ray cavities and associated sound waves, it is potentially easy to confuse these ripples with shock waves stemming from merger events. To demonstrate this danger in interpreting observations, we here analyse a specific case where the presence of smaller systems passing through the cluster might induce such a misleading conclusion.

To this end, we computed projected maps of the S2 galaxy cluster without AGN heating at  $z = 0.13$ . At this time, two substructures at radial distances of about half the virial radius are moving towards the centre. These substructures are still visible in the gas density map (upper right panel of Figure 14), but almost completely vanish when the X-ray luminosity map is computed. Nevertheless, when the unsharp masking procedure is applied to the  $L_X$  map, a two-lobed feature is clearly visible (upper left panel of Figure 14). Even though this feature at first glance looks strikingly similar to the ripples produced by bubble heating events, it is exclusively a product of the specific spatial geometry of the substructures in the cluster, and is also enhanced due to projection effects.

In the mass-weighted temperature map (lower left panel of Figure 14), two spherical regions can be noticed that are slightly cooler than their surroundings. They correspond to the two substructures. Especially around the substructure in

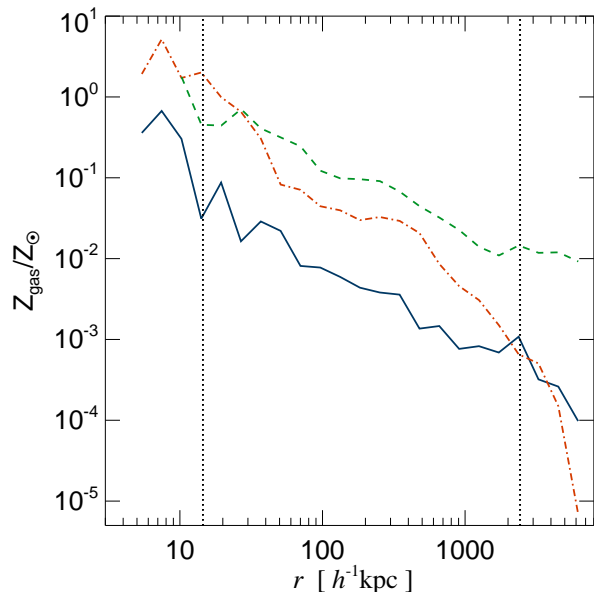


**Figure 12.** Radial profiles of the gas metallicity of the S1 galaxy cluster. Only the diffuse hot gas component has been used to estimate the metallicity, which is given in Solar units. The blue solid line is for the run without AGN heating, the red dot-dashed line is for bubble injection based on our “Magorrian model”, while the green dashed line is also for the “Magorrian model” but with additional inclusion of feedback by galactic winds. We can see that the feedback processes manage to better spread the metals into the diffuse ICM gas, and the increased mixing leads to a less clumpy metallicity distribution.

the lower right part of the map, hotter surrounding gas can be seen. To distinguish between a cold front or a shock, we can analyse the pressure of the surrounding gas and compute the Mach number map<sup>§</sup> (lower right panel of Figure 14). A clear jump of pressure in the region adjacent to the hot gas around the substructure together with the mildly supersonic motion of the substructure indicates the presence of weak shocks. Note that these shocks cannot be easily identified observationally as being caused by infalling substructures. Thus, if a careful analysis is not performed, these features could be associated mistakenly with sound waves caused by AGN bubbles, especially if at the same time some fossil but unrelated bubble is detected in the cluster by its radio emission.

#### 4.6 AGN heating in galaxy clusters of different mass

Here we discuss the effect of AGN heating in clusters spanning a wide range in mass, following their cosmological evolution up to  $z = 0$ . Their main properties are summarized in Tables 2 and 3. We analyze how the gas properties of

<sup>§</sup> We made a crude estimate of the Mach number by calculating for every gas particle its velocity in the galaxy cluster reference frame and dividing it by the local sound speed.

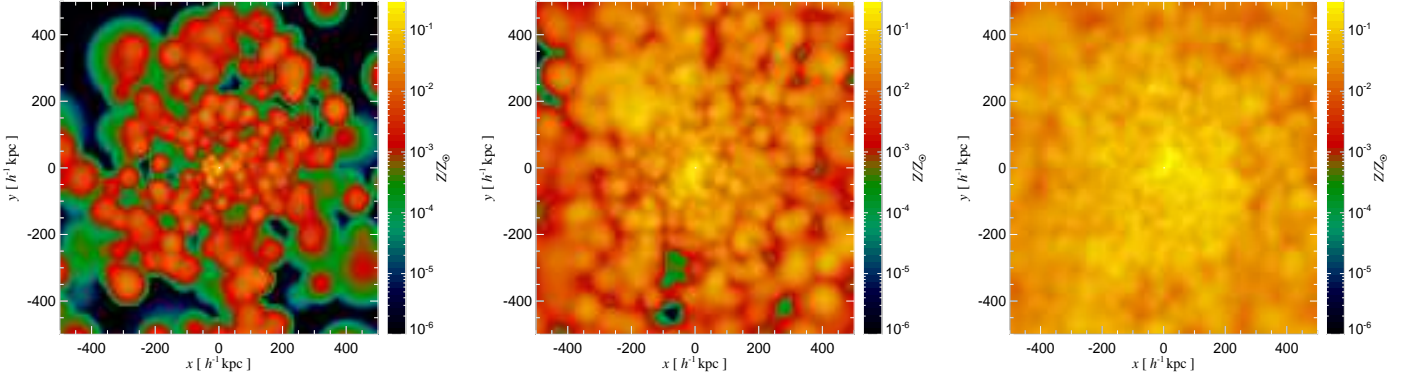


**Figure 13.** Mass-weighted gas metallicity maps of the S1 galaxy cluster at  $z = 0$ . The left panel corresponds to the case with cooling and star formation only. The middle panel shows how the metallicity of the hot gas component changes when AGN heating (here the “Magorrian model” was assumed) is included, while the right panel illustrates the case where in addition galactic winds with a velocity of  $\sim 480 \text{ km s}^{-1}$  were included, making the metallicity distribution more homogeneous.

clusters of different mass and at various radii, normalized to  $R_{200}$ , change due to the AGN-driven bubbles.

In Figure 15, we show for all clusters in our sample at  $z = 0$  the cumulative X-ray luminosity and mean gas temperature at four different radii,  $r = 0.03 R_{200}$ ,  $0.1 R_{200}$ ,  $0.5 R_{200}$  and  $R_{200}$ , marked with different colours and symbols. In this  $L_X - T$  plane, clusters are found at different places according to their mass, with less massive systems being located in the lower-left part of the panel and more massive ones in the upper-right part, as indicated in the figure. Also, cluster luminosity and temperature vary systematically with increasing radius  $r$ , with values at the virial radius occupying the upper-left part of the plot. The arrows attached to each cluster model show how  $L_X$  and  $T$  change when bubble heating is present. Clearly, there is a systematic trend of decreasing X-ray luminosity for all clusters and at all considered radii. This effect is more pronounced in the most inner regions and it is important both for massive clusters and smaller systems. Thus, in the cosmological simulations the bubble heating efficiency is not as clearly related to the mass of the host cluster as is the case for the isolated halos. From Figure 15, it can be seen that the two low mass clusters exhibit prominent imprints caused by AGN activity, highlighting that the bubble heating is more complex in cosmological simulations due to the hierarchical merging histories of clusters.

The gas temperature does not follow an equally clear trend as  $L_X$  for all the clusters in our sample, but in most cases, and especially for central clusters regions, it is boosted towards higher values, implying that bubble injection leads to an effective heating of the ICM. These trends in  $L_X$  and  $T$  confirm our previous findings for the S1/S2 clusters (presented in Figure 9), and show that they are general features of our AGN heating model. Interestingly, recent observational work by Croston et al. (2005) indicates that radio-loud elliptical-dominated groups have  $L_X - T$  scaling relations systematically different from those of elliptical-dominated radio-quiet groups. Their observed trends in the  $L_X - T$  plane are qualitatively similar with what we find, showing that for a given X-ray luminosity radio-loud groups have systematically higher gas temperature values. Never-

theless, since they are probing smaller mass systems, simulated galaxy groups with a matching range in mass are needed in order to make a more detailed comparison. Recent observational works (McNamara et al., 2005; Nulsen et al., 2005a) revealed the presence of very powerful outbursts due to the AGN activity, which are also accompanied with large-scale shocks. These clusters are located above the mean  $L_X - T$  relation, probably because we are witnessing the very early stages of bubble feedback, where pressure equilibrium with the surrounding ICM has not yet been established.

## 5 DISCUSSION AND CONCLUSIONS

In this work, we discussed a simulation model for AGN heating in the form of hot, buoyant bubbles, which are inflated by active phases of supermassive black holes at the centres of massive halos. The motivation for such a mode of feedback stems from the rich phenomenology of X-ray cavities and radio bubbles observed in clusters of galaxies, and the suggestion that this AGN activity may represent the solution of the ‘cooling flow puzzle’ posed by clusters of galaxies.

Several previous studies in the literature (e.g. Churazov et al., 2001; Quilis et al., 2001; Brüggén, 2003; Hoefl & Brüggén, 2004; Dalla Vecchia et al., 2004) have analysed bubble feedback in isolated galaxy clusters using hydrodynamical mesh codes. We here present the first implementation of this feedback in a SPH code, so an important goal was to test whether our results are consistent with these previous studies based on very different hydrodynamical techniques. Reassuringly, this is the case, both qualitatively and quantitatively. In particular, for galaxy clusters of similar masses as considered by Quilis et al. (2001); Dalla Vecchia et al. (2004), and with bubbles parametrised in an analogous way, we find changes induced by AGN-heating in gas properties, e.g. density and temperature radial profiles, central mass deposition rates, that are in excellent agreement. Also, the morphology of the bubbles and their time evolution are very similar. This is important because it implies that the SPH technique, which is more easily applicable to full blown cos-

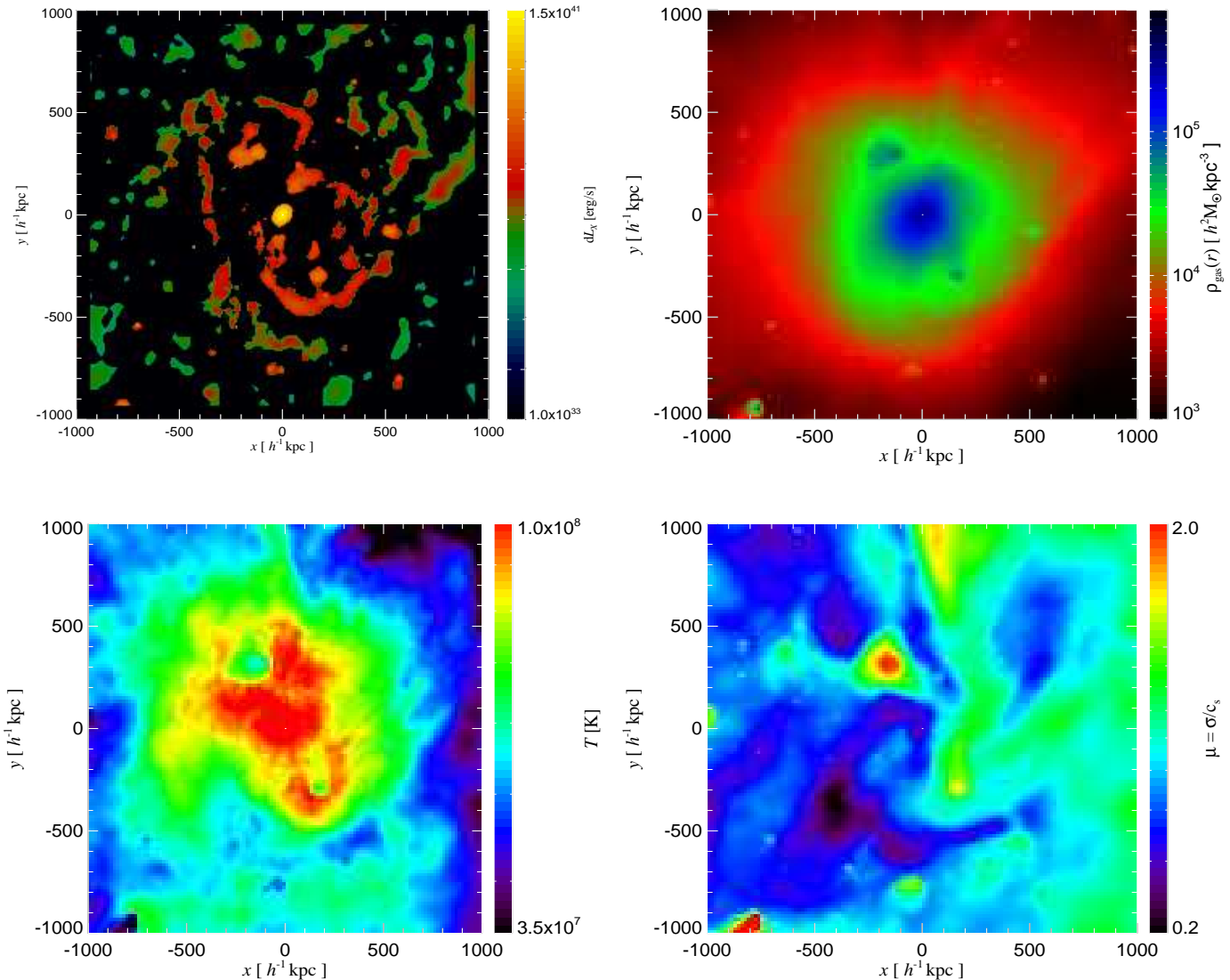


**Figure 14.** Projected maps of different gas properties of the S2 galaxy cluster at  $z = 0.13$ , where a merger with two smaller subclumps is in progress. AGN heating has not been included in this simulation. The upper left panel shows the unsharp masked image of the X-ray luminosity on a scale of  $160 h^{-1} \text{kpc}$ , and the upper right panel illustrates the gas density map. On the lower left panel we show a map of mass-weighted cluster gas temperature, while the lower right panel gives a crude estimate of the mass-weighted Mach number.

mological simulations of cluster formation, can be reliably used to study bubble feedback.

In our simulations, we considered both, isolated halos of different mass, and cosmological simulations of the  $\Lambda\text{CDM}$  model that follow galaxy cluster assembly from high redshift to the present. The isolated simulations served as a laboratory to study the dynamics of bubbles in detail. By considering halos with masses ranging from  $10^{12} h^{-1} M_{\odot}$  to  $10^{15} h^{-1} M_{\odot}$ , they also allowed us to gain some insight in how the coupling of radiative cooling to the AGN heating varies with cluster mass. An important conclusion from these experiments is that for systems of mass lower than  $\sim 10^{13} h^{-1} M_{\odot}$  bubbles with reasonable energy content are not capable of preventing excessive gas cooling. If one nevertheless allows for very large energy in these systems, a stable suppression of the cooling requires a delicate fine tuning of

the bubbles. However, the inefficiency of bubble heating in lower mass systems is also caused in part by our injection prescription, which is based on global properties of the host galaxy cluster without accounting for the actual amount of cooling gas present in the very centre.

In our cosmological simulations, we find that bubble injection can substantially affect galaxy cluster properties, especially in massive, relaxed clusters and at late cosmological times. Central cluster gas is efficiently heated, and thus both the amount of cold baryons and the star formation in the central cD galaxy is reduced. Also, an excessive mass deposition rate by cooling flows is prevented. AGN-driven bubbles not only modify the properties of the most central cluster parts, but alter the whole inner region of massive clusters, out to radii of order  $\sim 300 h^{-1} \text{kpc}$ , where the gas density is reduced and the temperature is increased. As a re-

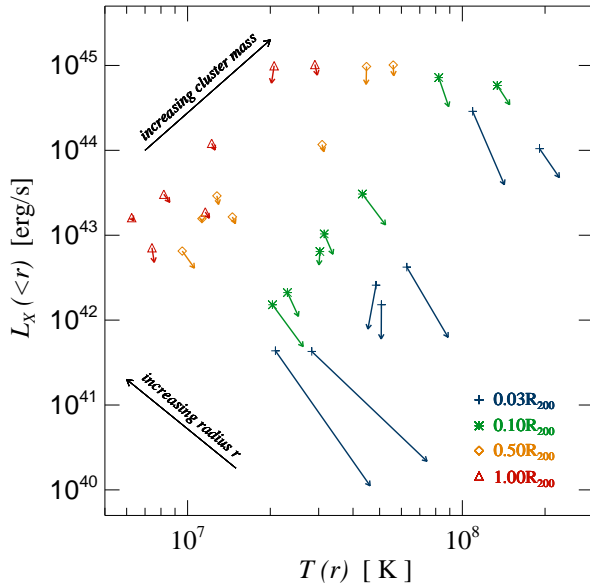


**Figure 15.** Cumulative X–ray luminosity of seven galaxy clusters as a function of their mass-weighted gas temperature. We give results for redshift  $z = 0$ , and at four different radii. Different symbols and colours denote estimates of  $L_X$  and  $T$  at different radii normalized to  $R_{200}$ : blue crosses correspond to  $0.03 R_{200}$ , green stars to  $0.1 R_{200}$ , yellow diamonds to  $0.5 R_{200}$ , and red triangles to  $R_{200}$ . The arrows indicate how the cluster luminosity and temperature change when AGN heating is included, i.e. systematically decreasing  $L_X$  for all the considered radii. More massive clusters are located in the upper-right part of the panel, while less massive systems are found in the lower-left corner of the figure, as indicated.

sult, the X–ray luminosity is considerably reduced, while the gas entropy exhibits a flat core in the central region. These trends are all in the direction required to reconcile hydrodynamical simulations of cluster formation in the  $\Lambda$ CDM model with observations of real galaxy clusters.

We tried several variants of our bubble model in order to explore the dependence of obtained results on the detailed assumptions made about how the energy is released in the bubbles. In particular, we compared an instantaneous injection of energy into the bubbles with a scheme where the energy is released over a certain period of time (from  $5 \times 10^7$  yrs to  $5 \times 10^8$  yrs), we imposed that the bubble particles should not cool during a given time interval (e.g.  $\sim 10^8$  yrs), we tried different spatial patterns for the bubble placement, and we also varied the initial epoch where our AGN heating started (from  $z = 6$  to  $z = 3$ ). None of these changes was really capable of modifying our results considerably. However, it appears that our findings are much more sensitive to the adopted model for the time evolution of the bubble energy. We explicitly demonstrated this by changing the rate at which the energy is released with time, under the constraint that the total energy injected from  $z = 3$  to  $z = 0$  was kept constant. When we linked the bubble energy content in this way to a model for the BH accretion rate, the fraction of cold gas and the star formation rate can

be noticeably reduced even at early times, but this is compensated by a reduced efficiency of bubble heating at late times, such that cooling flows are not suppressed sufficiently at  $z = 0$ . The “Magorrian model”, where the feedback occurs primarily at low redshift fares better in this respect, and gives therefore a better match to the properties of observed rich clusters of galaxies. In addition, we explored yet another scaling between the energy of the bubbles and the mass of the host galaxy cluster, namely  $E_{\text{bub}} \propto M_{200}^{5/3}$ , which can be motivated by the observed  $M_{\text{BH}} - \sigma$  relation as well. Also, Ferrarese & Ford (2005) pointed out a relationship between the mass of the black hole, in the form of  $M_{\text{BH}} \propto M_{\text{DM}}^{1.65}$ . Thus, if the energy content of the bubbles is a linear function of the black hole mass, the above scaling is obtained. One also arrives at  $E_{\text{bub}} \propto M_{200}^{5/3}$  if one assumes that the energy in the bubbles is some small fraction of the total thermal cluster energy, which roughly scales as  $M_{200}^{5/3}$ . In performing the analysis with the modified slope, we fixed the normalization of the  $E_{\text{bub}} \propto M_{200}^{5/3}$  relation at redshift  $z = 0$  to be equal to the value in our ordinary “Magorrian model”. The results of this analysis showed that the change in the slope from  $4/3$  to  $5/3$  produces qualitatively very similar results, and hence it follows that the properties of our simulated galaxy clusters are not very sensitive to such a modest change of the AGN heating prescription.

In the newly emerging picture for the joint evolution of galaxies and supermassive black holes, the interplay between AGN and their host galaxies may be composed of two modes. One mode is caused by the quiescent accretion of intracluster gas onto the central BH, provoking periodic AGN activity which manifests itself in jets and radio bubbles. This mode plays a more important role at late cosmological epochs, in massive and more relaxed systems, and it is often referred to as a “radio-mode” (e.g. Croton et al., 2005). The other mode occurs in merging pairs of galaxies, where strong tidal forces efficiently funnel large amounts of cold gas towards the nuclei of the merging galaxies, where it becomes available for fueling the embedded supermassive BHs (Di Matteo et al., 2005; Springel et al., 2005b). The associated intense accretion triggers quasar activity, which is more frequent at higher redshift due to the larger merger rates there. If a small fraction of the bolometric luminosity of the quasar couples thermally to the surrounding gas, a prominent gas outflow can eventually be created during the formation of ellipticals, which then shuts off further accretion and star formation (Springel et al., 2005a) and establishes the  $M_{\text{BH}} - \sigma$  relationship (Di Matteo et al., 2005).

The latter process, the ‘quasar mode’, has already been explored in direct simulation models of galaxy mergers, but not yet in cosmological simulations. It would therefore be extremely interesting to couple these two modes of AGN feedback in a unified simulation model for supermassive black hole growth, and to carry out cosmological simulations with it. In such a model, the energetics of the bubbles and the periods of AGN activity can then be made directly dependent on the current BH mass and on the local physics of accreting gas, removing much of the freedom in our present bubble models. We will present such a model in forthcoming work. In addition, our work suggests that for a more complete picture of the ICM dynamics, additional physical processes should be incorporated as well. This includes thermal con-

duction, even though it is probably relevant only in the most massive systems. We also suggest that the physical viscosity expected for the ICM gas should be considered as well, since the efficiency of non-local AGN heating by viscous dissipation of sound waves will depend crucially on this input. Finally, radio observations strongly suggest that bubbles are prevalently filled with relativistic particles, which appear as radio lobes, and in many cases are coincident with X-ray cavities. Therefore, it would be important to address, using fully cosmological simulation of cluster formation, the role of non-thermal radio plasma in bubbles for heating of the ICM. It appears that for some time to come clusters of galaxies will remain one of the most interesting places to study complex hydrodynamic phenomena in the Universe.

## ACKNOWLEDGEMENTS

We thank Martin Jubelgas for providing a code to set-up isolated halos in equilibrium, Elena Rasia for help in producing mock observations with X-MAS, and Klaus Dolag for providing cluster initial conditions. We are indebted to Simon White and Eugene Churazov for very useful comments on the manuscript. DS acknowledges the PhD fellowship of the International Max Planck Research School in Astrophysics, and received support from Marie Curie Host Fellowship for Early Stage Research Training.

## REFERENCES

- Allen S. W., 2000, *MNRAS*, 315, 269
- Allen S. W., Fabian A. C., Edge A. C., Bohringer H., White D. A., 1995, *MNRAS*, 275, 741
- Allen S. W., Fabian A. C., Johnstone R. M., Arnaud K. A., Nulsen P. E. J., 2001a, *MNRAS*, 322, 589
- Allen S. W., Schmidt R. W., Fabian A. C., 2001b, *MNRAS*, 328, L37
- Birzan L., Rafferty D. A., McNamara B. R., Wise M. W., Nulsen P. E. J., 2004, *ApJ*, 607, 800
- Böhringer H., Matsushita K., Churazov E., Finoguenov A., Ikebe Y., 2004, *A&A*, 416, L21
- Böhringer H., Matsushita K., Churazov E., Ikebe Y., Chen Y., 2002, *A&A*, 382, 804
- Babul A., Balogh M. L., Lewis G. F., Poole G. B., 2002, *MNRAS*, 330, 329
- Balogh M. L., Pearce F. R., Bower R. G., Kay S. T., 2001, *MNRAS*, 326, 1228
- Blanton E. L., Sarazin C. L., McNamara B. R., Wise M. W., 2001, *ApJ*, 558, L15
- Borgani S., Governato F., Wadsley J., et al., 2001, *ApJ*, 559, L71
- Borgani S., Murante G., Springel V., et al., 2004, *MNRAS*, 348, 1078
- Bower R. G., 1997, *MNRAS*, 288, 355
- Brüggen M., 2003, *ApJ*, 592, 839
- Brüggen M., Kaiser C. R., 2002, *Nature*, 418, 301
- Brüggen M., Kaiser C. R., Churazov E., Enßlin T. A., 2002, *MNRAS*, 331, 545
- Brüggen M., Ruszkowski M., Hallman E., 2005, *ApJ*, 630, 740
- Bruzual G., Charlot S., 2003, *MNRAS*, 344, 1000
- Churazov E., Brüggen M., Kaiser C. R., Böhringer H., Forman W., 2001, *ApJ*, 554, 261
- Churazov E., Sazonov S., Sunyaev R., Forman W., Jones C., Böhringer H., 2005, *MNRAS*, 363, L91
- Churazov E., Sunyaev R., Forman W., Böhringer H., 2002, *MNRAS*, 332, 729
- Cowie L. L., Binney J., 1977, *ApJ*, 215, 723
- Croston J. H., Hardcastle M. J., Birkinshaw M., 2005, *MNRAS*, 357, 279
- Croton D. J., Springel V., White S. D. M., et al., 2005, *MNRAS*, 1055+
- Dalla Vecchia C., Bower R. G., Theuns T., Balogh M. L., Mazzotta P., Frenk C. S., 2004, *mnras*, submitted (preprint astro-ph/0402441)
- De Grandi S., Etti S., Longhetti M., Molendi S., 2004, *A&A*, 419, 7
- De Grandi S., Molendi S., 2002, *ApJ*, 567, 163
- Di Matteo T., Croft R. A. C., Springel V., Hernquist L., 2003, *ApJ*, 593, 56
- Di Matteo T., Springel V., Hernquist L., 2005, *Nature*, 433, 604
- Dolag K., 2004, in *The Riddle of Cooling Flows in Galaxies and Clusters of galaxies*
- Dolag K., Jubelgas M., Springel V., Borgani S., Rasia E., 2004, *ApJ*, 606, L97
- Donahue M., Voit G. M., O’Dea C. P., Baum S. A., Sparks W. B., 2005, *ApJ*, 630, L13
- Edge A. C., 2001, *MNRAS*, 328, 762
- Edge A. C., Frayer D. T., 2003, *ApJ*, 594, L13
- Edge A. C., Wilman R. J., Johnstone R. M., Crawford C. S., Fabian A. C., Allen S. W., 2002, *MNRAS*, 337, 49
- Ensslin T. A., Vogt C., 2005, *ArXiv Astrophysics e-prints*, astro-ph/0505517
- Fabian A. C., 1994, *ARA&A*, 32, 277
- Fabian A. C., Mushotzky R. F., Nulsen P. E. J., Peterson J. R., 2001, *MNRAS*, 321, L20
- Fabian A. C., Nulsen P. E. J., 1977, *MNRAS*, 180, 479
- Fabian A. C., Nulsen P. E. J., Canizares C. R., 1984, *Nature*, 310, 733
- Fabian A. C., Sanders J. S., Allen S. W., et al., 2003a, *MNRAS*, 344, L43
- Fabian A. C., Sanders J. S., Crawford C. S., Conselice C. J., Gallagher J. S., Wyse R. F. G., 2003b, *MNRAS*, 344, L48
- Fabian A. C., Sanders J. S., Etti S., et al., 2000, *MNRAS*, 318, L65
- Ferrarese L., Ford H., 2005, *Space Science Reviews*, 116, 523
- Gardini A., Rasia E., Mazzotta P., Tormen G., De Grandi S., Moscardini L., 2004, *MNRAS*, 351, 505
- Hoefl M., Brüggen M., 2004, *ApJ*, 617, 896
- Jenkins A., Frenk C. S., White S. D. M., et al., 2001, *MNRAS*, 321, 372
- Johnstone R. M., Fabian A. C., Nulsen P. E. J., 1987, *MNRAS*, 224, 75
- Jubelgas M., Springel V., Dolag K., 2004, *MNRAS*, 351, 423
- Kaastra J. S., Ferrigno C., Tamura T., Paerels F. B. S., Peterson J. R., Mittaz J. P. D., 2001, *A&A*, 365, L99
- Kaiser N., 1986, *MNRAS*, 222, 323
- Kaiser N., 1991, *ApJ*, 383, 104
- Katz N., Weinberg D. H., Hernquist L., 1996, *ApJS*, 105, 19
- Kauffmann G., Colberg J. M., Diaferio A., White S. D. M., 1999, *MNRAS*, 303, 188
- Lewis G. F., Babul A., Katz N., Quinn T., Hernquist L., Weinberg D. H., 2000, *ApJ*, 536, 623
- Markevitch M., Vikhlinin A., Mazzotta P., 2001, *ApJ*, 562, L153
- Mazzotta P., Kaastra J. S., Paerels F. B., et al., 2002, *ApJ*, 567, L37
- McCarthy I. G., Balogh M. L., Babul A., Poole G. B., Horner D. J., 2004, *ApJ*, accepted (preprint astro-ph/0406329)
- McNamara B. R., Nulsen P. E. J., Wise M. W., et al., 2005, *Nature*, 433, 45
- McNamara B. R., Wise M., Nulsen P. E. J., et al., 2000, *ApJ*, 534, L135
- Muanwong O., Thomas P. A., Kay S. T., Pearce F. R., Couchman H. M. P., 2001, *ApJ*, 552, L27
- Narayan R., Medvedev M. V., 2001, *ApJ*, 562, L129

- Navarro J. F., Frenk C. S., White S. D. M., 1995, *MNRAS*, 275, 720
- Navarro J. F., Frenk C. S., White S. D. M., 1996, *ApJ*, 462, 563
- Navarro J. F., Frenk C. S., White S. D. M., 1997, *ApJ*, 490, 493
- Nulsen P. E., McNamara B. R., David L. P., Wise M., 2003, *The Cosmic Cauldron*, 25th meeting of the IAU, Joint Discussion 10, 18 July 2003, Sydney, Australia, 10
- Nulsen P. E. J., Hambrick D. C., McNamara B. R., et al., 2005a, *ApJ*, 625, L9
- Nulsen P. E. J., McNamara B. R., Wise M. W., David L. P., 2005b, *ApJ*, 628, 629
- O'Connell R. W., McNamara B. R., 1989, *AJ*, 98, 180
- Oh S. P., Benson A. J., 2003, *MNRAS*, 342, 664
- Owen F. N., Eilek J. A., Kassim N. E., 2000, *ApJ*, 543, 611
- Peterson J. R., Kahn S. M., Paerels F. B. S., et al., 2003, *ApJ*, 590, 207
- Peterson J. R., Paerels F. B. S., Kaastra J. S., et al., 2001, *A&A*, 365, L104
- Quilis V., Bower R. G., Balogh M. L., 2001, *MNRAS*, 328, 1091
- Reynolds C. S., McKernan B., Fabian A. C., Stone J. M., Vernaleo J. C., 2005, *MNRAS*, 357, 242
- Ruszkowski M., Begelman M. C., 2002, *ApJ*, 581, 223
- Ruszkowski M., Brüggem M., Begelman M. C., 2004, *ApJ*, 615, 675
- Salomé P., Combes F., 2004, *A&A*, 415, L1
- Sanders J. S., Fabian A. C., 2002, *MNRAS*, 331, 273
- Sanderson A. J. R., Finoguenov A., Mohr J. J., 2005, *ApJ*, 630, 191
- Sarazin C. L., 1988, *X-ray emission from clusters of galaxies*, Cambridge Astrophysics Series, Cambridge: Cambridge University Press, 1988
- Springel V., 2005, *MNRAS*, submitted (preprint astro-ph/0505010)
- Springel V., Di Matteo T., Hernquist L., 2005a, *ApJ*, 620, L79
- Springel V., Di Matteo T., Hernquist L., 2005b, *MNRAS*, 361, 776
- Springel V., Hernquist L., 2002, *MNRAS*, 333, 649
- Springel V., Hernquist L., 2003, *MNRAS*, 339, 289
- Springel V., White S. D. M., Tormen G., Kauffmann G., 2001a, *MNRAS*, 328, 726
- Springel V., Yoshida N., White S. D. M., 2001b, *New Astronomy*, 6, 79
- Tamura T., Kaastra J. S., Peterson J. R., et al., 2001, *A&A*, 365, L87
- Tormen G., Bouchet F. R., White S. D. M., 1997, *MNRAS*, 286, 865
- Tornatore L., Borgani S., Springel V., Matteucci F., Menci N., Murante G., 2003, *MNRAS*, 342, 1025
- Tozzi P., Norman C., 2001, *ApJ*, 546, 63
- Tremaine S., Gebhardt K., Bender R., et al., 2002, *ApJ*, 574, 740
- Voigt L. M., Fabian A. C., 2003, *MNRAS*, submitted (preprint astro-ph/0308352)
- Voigt L. M., Schmidt R. W., Fabian A. C., Allen S. W., Johnstone R. M., 2002, *MNRAS*, 335, L7
- Voit G. M., 2004, *ArXiv Astrophysics e-prints*, astro-ph/0410173
- Voit G. M., Balogh M. L., Bower R. G., Lacey C. G., Bryan G. L., 2003, *ApJ*, 593, 272
- Voit G. M., Bryan G. L., 2001, *Nature*, 414, 425
- Voit G. M., Bryan G. L., Balogh M. L., Bower R. G., 2002, *ApJ*, 576, 601
- Voit G. M., Donahue M., 2005, *ArXiv Astrophysics e-prints*, astro-ph/0509176
- White D. A., Fabian A. C., Allen S. W., et al., 1994, *MNRAS*, 269, 589
- White D. A., Jones C., Forman W., 1997, *MNRAS*, 292, 419
- White S. D. M., Navarro J. F., Evrard A. E., Frenk C. S., 1993, *Nature*, 366, 429
- Wu X., Xue Y., 2002, *ApJ*, 572, L19
- Yoshida N., Sheth R. K., Diaferio A., 2001, *MNRAS*, 328, 669
- Yoshida N., Stoehr F., Springel V., White S. D. M., 2002, *MNRAS*, 335, 762
- Zakamska N. L., Narayan R., 2003, *ApJ*, 582, 162